GEOFLUIDS

Geofluids (2014) **14**, 391–418 doi: 10.1111/gfl.12083

Changes in fluid pathways in a calcite vein mesh (Natih Formation, Oman Mountains): insights from stable isotopes

M. ARNDT[1], S. VIRGO[1], S. F. COX[2] AND J. L. URAI[1,3]

[1]*Structural Geology, Tectonics and Geomechanics, Energy and Mineral Resources Group (EMR), RWTH Aachen University, Lochnerstrasse 4-20, 52056, Aachen, Germany;* [2]*Research School of Earth Sciences, The Australian National University, Canberra, ACT, Australia;* [3]*German University of Technology, GUtech, Muscat, Oman*

ABSTRACT

We present a structural, microstructural, and stable isotope study of a calcite vein mesh within the Cretaceous Natih Formation in the Oman Mountains to explore changes in fluid pathways during vein formation. Stage 1 veins form a mesh of steeply dipping crack-seal extension veins confined to a 3.5-m-thick stratigraphic interval. Different strike orientations of Stage 1 veins show mutually crosscutting relationships. Stage 2 veins occur in the dilatant parts of a younger normal fault interpreted to penetrate the stratigraphy below. The $\delta^{18}O$ composition of the host rock ranges from 21.8‰ to 23.7‰. The $\delta^{13}C$ composition ranges from 1.5‰ to 2.3‰. This range is consistent with regionally developed diagenetic alteration at top of the Natih Formation. The $\delta^{18}O$ composition of vein calcite varies from 22.5‰ to 26.2‰, whereas $\delta^{13}C$ composition ranges from −0.8‰ to 2.1‰. A first trend observed in Stage 1 veins involves a decrease of $\delta^{13}C$ to compositions nearly 1.3‰ lower than the host rock, whereas $\delta^{18}O$ remains constant. A second trend observed in Stage 2 calcite has $\delta^{18}O$ values up to 3.3‰ higher than the host rock, whereas the $\delta^{13}C$ composition is similar. Stable isotope data and microstructures indicate an episodic flow regime for both stages. During Stage 1, formation of a stratabound vein mesh involved bedding-parallel flow, under near-lithostatic fluid pressures. The ^{18}O fluid composition was host rock-buffered, whereas ^{13}C composition was relatively depleted. This may reflect reaction of low ^{13}C CO_2 derived by fluid interaction with organic matter in the limestones. Stage 2 vein formation is associated with fault-controlled fluid flow accessing fluids in equilibrium with limestones about 50 m beneath. We highlight how evolution of effective stress states and the growth of faults influence the hydraulic connectivity in fracture networks and we demonstrate the value of stable isotopes in tracking changes in fluid pathways.

Key words: calcite veins, carbonate reservoirs, crack-seal microstructures, dynamic fracture permeability, episodic fluid flow, fluid flow regimes, fracture sealing, Natih Formation, Oman Mountains, overpressures, stable isotopes, vein meshes

Received 14 August 2013; accepted 30 April 2014

Corresponding author: Max Arndt, RWTH-Aachen University, Structural Geology, Tectonics and Geomechanics, Lochnerstraße 4-20, D-52056 Aachen, Germany. Email: m.arndt@ged.rwth-aachen.de. Tel: +49 241 8095723. Fax: +49 241 8092358.

Geofluids (2014) **14**, 391–418

INTRODUCTION

Fluid flow and isotope exchange in fractured reservoirs

Growth of fracture meshes (networks) in deeply buried, low-permeability sedimentary rock sequences during crustal deformation plays a critical role in generating fluid pathways and facilitates fluid redistribution between various crustal reservoirs. Isotopic studies of veins formed by precipitation of minerals from fluids in these meshes can provide a powerful tool for exploring scales of mass transfer and structural control on high fluid–flux pathways (e.g., Dietrich *et al.* 1983; Rye & Bradbury 1988; Cartwright *et al.* 1994; Abart *et al.* 2002; Knoop *et al.* 2002; Agosta & Kirschner 2003; Lefticariu *et al.* 2005; Cox 2007).

In actively deforming regions, fluid pathways in fracture networks are governed by the dimensions of fractures and the evolution of connectivity in an array of fractures between the upstream and downstream parts of flow systems. As fractures tend to be short and isolated from each other during the early stages of growth of fracture networks (Barnhoorn *et al.* 2010), vein sealing at this stage is

dominated by diffusional mass transfer through the fluid or by short-range advective fluid redistribution. Such veins tend to have an isotopic composition that reflects buffering by the host rock. As fracture networks grow, they may propagate along the mechanical stratigraphy, producing 'stratabound' networks. As long as fluid circulation is tightly stratabound, fluid composition will be buffered by the composition of the immediate host rock. However, growing fracture networks may also propagate across stratigraphy and thereby provide pathways for fluid migration between rocks of differing isotopic composition. In this case, fluid composition recorded by veins may be influenced by externally sourced fluids, buffered by host rocks further upstream on the flow path. Transitions from rock-buffered conditions to more fluid-buffered conditions, as connectivity in vein meshes evolves, have been recorded in isotopic studies of some veins (e.g., Dietrich *et al.* 1983; Rye & Bradbury 1988; Lefticariu *et al.* 2005; Cox 2007).

At temperatures below approximately 250°C, isotopic exchange in carbonates between the fluid and the solid phase is related to dissolution and precipitation processes (Hudson 1977; Valley & O'Neil 1981). As externally buffered fluids react progressively with rocks of a particular isotopic composition along a flow path, they become more rock-buffered toward the downstream parts of the system. How closely rock-buffered a fluid becomes is dependent on many parameters, but particularly on path length, fluid flow rate, total fluid flux, and kinetics of isotopic exchange between fluid and reactive host rocks (Lassey & Blattner 1988). Reactive transport modeling of isotopic profiles in veins and host rocks along flow paths can be used to constrain flow direction and fluid flux (e.g., Lassey & Blattner 1988; Bowman *et al.* 1994; Barnett & Bowman 1995; Gerdes *et al.* 1995; McCaig *et al.* 1995; Abart & Sperb 1997; Abart & Pozzorini 2000; Knoop *et al.* 2002; Cox 2007). The isotopic composition of vein minerals formed during the growth of vein networks may preserve a record of changes in fluid chemistry during the evolution of a flow system (Dietrich *et al.* 1983; Rye & Bradbury 1988; Cox 2007). Accordingly, the integration of stable isotope data from incrementally grown veins, with understanding of deformational control on the development of fluid pathways and their permeability history, offers potential to explore the dynamics of coupling between growth of fracture networks, fluid migration, and fluid–rock interaction during crustal deformation.

Vein meshes in thrust belts

Vein meshes have been studied extensively in thrust belts with respect to their structure, morphology, geochemistry, burial history, and p–T conditions during vein formation. Sibson (1996) studied earthquake (fault)-related meshes, with simultaneous fracture formation, where the individual mesh segments are open for fluid flow at the same time. Holland & Urai (2010) described crack-seal vein meshes, where the mesh developed as successive vein generations. Vein meshes in thrust belts can be stratabound (Odling *et al.* 1999; Van Noten *et al.* 2012), or cut vertically through the stratigraphy (cf. Sibson 1996; Eichhubl & Boles 2000). They can form at great depth (Lefticariu *et al.* 2005; Van Noten *et al.* 2012) or in shallow settings (Rygel *et al.* 2006; see also Sibson 1996). Fluid pressures during formation of vein meshes can be near-lithostatic (Rygel *et al.* 2006; Van Noten *et al.* 2012) to hydrostatic (Eichhubl & Boles 2000; Wiltschko *et al.* 2009; see also Sibson 1996; Oliver & Bons 2001 and references therein). Their structural position varies widely and can be in the footwall (Dietrich *et al.* 1983; Wiltschko *et al.* 2009) or in the hanging wall of major thrusts (Rygel *et al.* 2006; Cooley *et al.* 2011). In addition, the spatial and temporal relation of vein mesh formation to folding is important (Lefticariu *et al.* 2005; Rygel *et al.* 2006; Wiltschko *et al.* 2009; Cooley *et al.* 2011; Van Noten *et al.* 2012). The origin of vein forming fluids can also vary widely. Fluids may originate locally from the host rocks (Dietrich *et al.* 1983; Wiltschko *et al.* 2009), but also fluid transport over large distances (i.e., meteoric water, basement fluids) has been widely recognized (Oliver & Bons 2001; Lefticariu *et al.* 2005; Rygel *et al.* 2006; Hilgers *et al.* 2006).

Microstructural processes in veins

Veins are produced by advection of fluid and/or local diffusional transport in fluid-filled fractures that become sealed by precipitation of dissolved material (Cox *et al.* 2001; Oliver & Bons 2001; Hilgers & Sindern 2005). The transport processes during vein formation are still debated (Bons *et al.* 2012). In low-permeability rocks, pervasive advective fluid flow (i.e., at the grain scale) is slow, and open fractures may be the major fluid pathways (Laubach *et al.* 2004; Laubach & Ward 2006). Material transport may also occur by diffusion along grain boundaries (Fisher 1951), especially in partially sealed veins that are not connected to advective fluid flow paths. It is widely accepted that more than one material transport process can be active during the development of a vein (Elburg *et al.* 2002; Bons *et al.* 2012).

Veins can form by multiple crack-seal events (Ramsay 1980) or by a single stage of opening and progressive sealing of a larger fracture. An alternative vein growth process involves the force of crystallization (Wiltschko & Morse 2001; Bons & Montenari 2005; Hilgers & Urai 2005; Matter & Kelemen 2009; Kelemen & Hirth 2012). During vein growth, the fracture walls are either overgrown epitaxially without nucleation (Hilgers *et al.* 2004), or by growth of newly nucleated crystals (Cox & Etheridge

1983; Urai *et al.* 2001; Bons *et al.* 2012). The latter process occurs where vein minerals are different from those present in the host rock (i.e., calcite crystals in slate; Urai *et al.* 1991; Hilgers & Sindern 2005; Hilgers & Urai 2005;). Epitaxial overgrowth is typical for systems, where the vein mineral is the same phase as the host rock phase (e.g., quartz veins in quartz-rich sandstone (Rickard & Rixon 1983; Urai *et al.* 2001; Van Noten *et al.* 2008) or calcite veins in limestone (Ramsay 1980; Dietrich *et al.* 1983; Kenis *et al.* 2000; Holland & Urai 2010).

During crack-seal growth, crystals can incorporate solid and/or fluid inclusions, which are commonly interpreted to mark opening events (Ramsay 1980; Cox & Etheridge 1983; Koehn & Passchier 2000; Renard *et al.* 2005). Crack-seal veins that grow outwards from their median zone are called antitaxial, whereas veins, which grow toward the vein interior, are called syntaxial (Durney & Ramsay 1973; Bons 2000). Both vein types require repeated and localized opening.

The efficiency of fluid–rock isotopic exchange during fracture-controlled flow is likely to be influenced by vein growth processes, especially when exchange is controlled by dissolution–precipitation processes. In syntaxial veins, direct isotopic exchange with the host rock is inhibited, because the fracture-filling fluid (passing through the interior of a vein) is shielded from the host rock by earlier vein fill. In antitaxial veins, direct fluid–rock isotopic exchange can occur with host rock during each fluid flow event. Where veins have a higher tensile strength than the host rock, new fractures form outside of preexisting veins (Caputo & Hancock 1998; Holland & Urai 2010). This fosters efficient fluid–rock isotopic exchange.

Aims

The main aim of this study is to integrate variations in C/O isotopic composition of veins, along with details of the internal structure of veins, to explore the mechanical, hydrological, and chemical processes and fluid pathways involved in the formation of calcite vein meshes (networks) in overpressured, fine-grained limestones. This study is the first attempt to integrate structural, microstructural, and C/O stable isotope data on calcite veins and their host rock in a rock volume of about 5×10^5 m^3 (50 m stratigraphic thickness × 100 m × 100 m laterally), to examine the evolution of a fracture-controlled, advective flow system that formed in overpressured autochthonous footwall carbonates that were overthrusted by allochthonous nappes in central Oman. The veins occur in a dense mesh and are exceptionally well exposed in an area of large, bedding-parallel pavements and adjacent cliffs. Spatial and temporal variations in C/O isotope composition of calcite veins and their limestone host rock are used to make inferences about the length scales of fluid transport during progressive deformation in the Oman Mountains. The study highlights how evolution of effective stress states and the growth of faults may influence the scale of hydraulic connectivity in fracture networks. It also demonstrates the value of stable isotopes in tracking changes in fluid pathways.

Geologic setting and previous work

We studied calcite veins hosted in limestones of the Natih Formation (Figs 1, 2 and 3) in exposures on the western flank of Jebel Shams in the Oman Mountains. The Cenomanian-Turonian (approx. 90–100 Ma) Natih Formation in Oman was subdivided by Hughes-Clarke (1988) into seven members (A–G). It is the topmost formation of the Cretaceous Wasia Group that forms the upper part of the Hajar Supergroup, also known as Autochthon B. The Hajar Supergroup comprises a 3-km-thick succession of carbonate rock that was deposited at the southern passive margin of the Neotethys from Late Permian (Wordian) to Late Cretaceous (Turonian) (Breton *et al.* 2004; Searle 2007). It unconformably overlies the Neoproterozoic–Ordovician basement (Autochthon A).

The top of the Natih Formation (member A) is unconformably overlain by the Muti Formation. The deposition of the Muti Formation reflects the transition from a passive continental margin to a foreland basin (Robertson 1987, 1988; Terken 1999; Al-Lazki *et al.* 2002; Searle 2007). It was deposited in a peripheral bulge that was caused by the south-directed obduction of allochthonous deep-sea sediments and oceanic lithosphere (Hawasina and Samail nappes) during the Late Cretaceous. Burial of the Mesozoic shelf sequence to depths of at least 7 km by the emplacement of the Hawasina and Samail nappes occurred at approximately 95–70 Ma (Searle 2007). The Muti Formation is a seal for hydrocarbon reservoirs in the Natih A oil fields of Oman's interior (Terken 1999; Al-Lazki *et al.* 2002; van Buchem *et al.* 2002). Its lower unit is composed of pelagic shales, carbonates, terrigenous turbidites, and limestone breccias (Robertson 1987; Rabu *et al.* 1990).

After nappe emplacement, several low-strain extensional and transpressional tectonic phases affected the region and were followed by growth of the Jebel Akhdar anticline, uplift, and erosion (Breton *et al.* 2004; Fournier *et al.* 2006; Hilgers *et al.* 2006; Al-Wardi & Butler 2007; Holland *et al.* 2009b; Virgo *et al.* 2013b; Gomez-Rivas et al. 2014). Oil is produced from Natih A limestone reservoirs in oil fields in the foreland (Fahud and Natih anticlines; Terken 1999). These limestones have porosities from 10% to 30%, whereas the limestones outcropping in the Jebel Akhdar window are compacted to very low porosity (Wagner 1990), in response to burial under the Hawasina and Samail nappe. Bitumen reflectance measurements

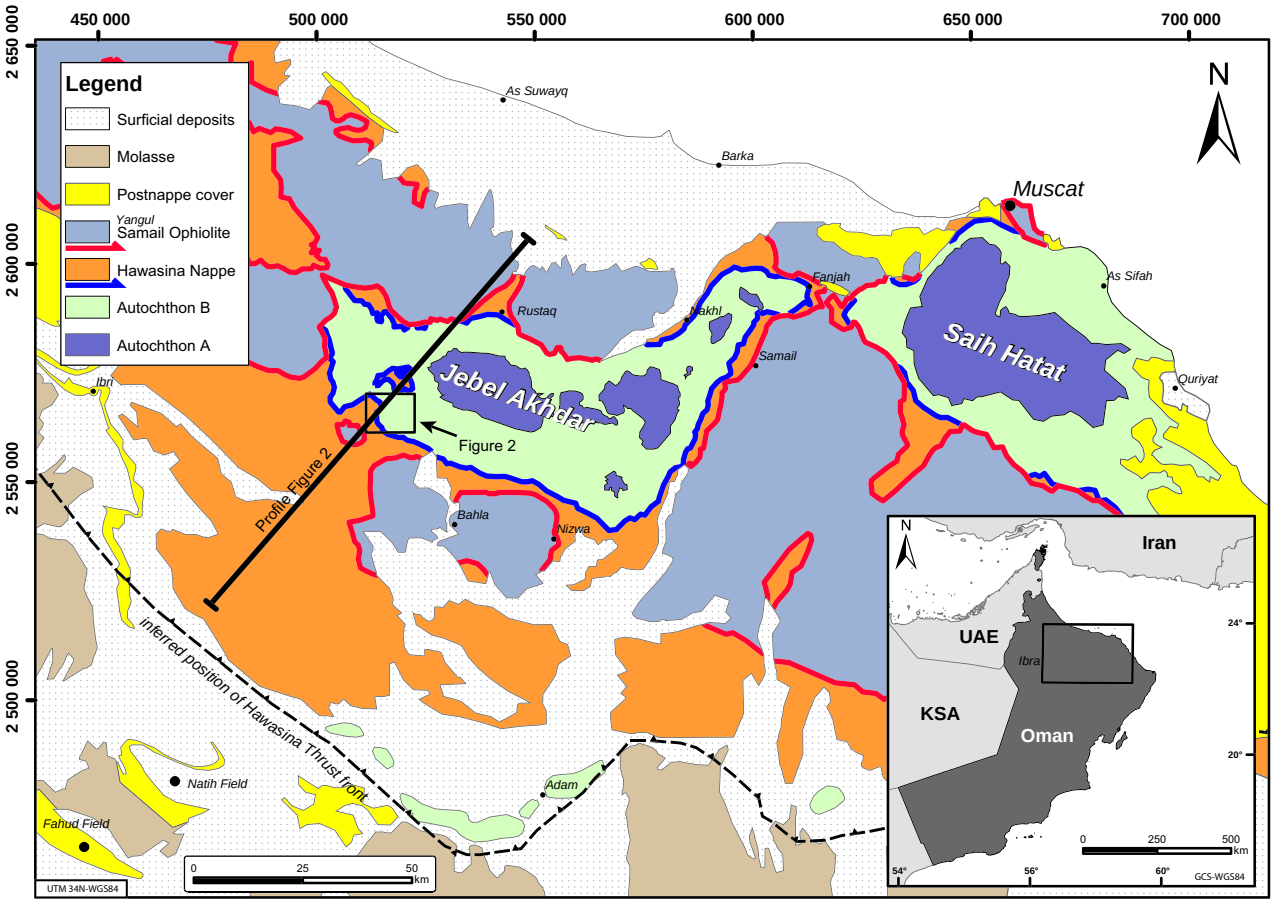

Fig. 1. Simplified geological map of Northern Oman. This study is focused on the Natih Formation within Autochthon B. The autochthon has been overridden by two major Nappes, the Hawasina and Samail Nappes during the Upper Cretaceous. The study area is situated on the southern limb of the Jebel Akhdar anticline. See Fig. 2 for details. Modified from Breton *et al.* (2004) and Searle (2007).

from the Natih B source rock (sequence III-4; cf. Wohlwend & Weissert 2012) in Wadi Nakhr (9 km SE of study area, Fig. 2) indicate peak temperatures between 200 and 240°C (Fink 2013).

In a regional structural and geochemical study on calcite veins in the autochthon of the Oman Mountains, Hilgers *et al.* (2006) described seven different vein sets and their stable isotope composition. While most of the early vein calcites have a largely rock-buffered signature, late, fault-related vein calcites are depleted in ^{18}O relative to their host rock. Hilgers *et al.* (2006) interpreted this as an indicator for meteoric water influx into deep reaching faults. Relatively high $\delta^{13}C$ values led to the interpretation that no significant amounts of hydrocarbons were present during vein formation. Hilgers *et al.* (2006) proposed that most veins formed in a high-pressure cell at close to lithostatic pressure, until the development of normal faults released the overpressures and meteoric fluids infiltrated the sequence.

Holland & Urai (2010) focused on thin, closely spaced crack-seal veins – termed 'zebra' veins. The stable isotope composition of the zebra veins has been found to be in equilibrium with their adjacent host rock. Holland *et al.* (2009a) described the vein systems of the Mesozoic limestones on the southern flank of Jebel Shams in detail and proposed a model for the structural evolution of the region. E-W-trending normal faulting and related veins were interpreted as the last vein-producing event in an area covering at least 30 square km adjacent to our study area. The work was aided by a remote sensing study mapping calcite-cemented normal faults, open joints, and veins (Holland *et al.* 2009b), using high-resolution satellite imagery of the same area. These studies were followed up by the high-resolution structural mapping of Virgo *et al.* (2013b). This study improved the remote sensing map of Holland *et al.* (2009b) and presented a more detailed model of the sequence of vein formation. It was concluded that veins at high angle to bedding first formed in the NNW strike direction. These veins were successively overprinted by veins at high angle to bedding, with various orientations. The vein sequence is consistent with an anticlockwise rotation of a horizontal minimum principal

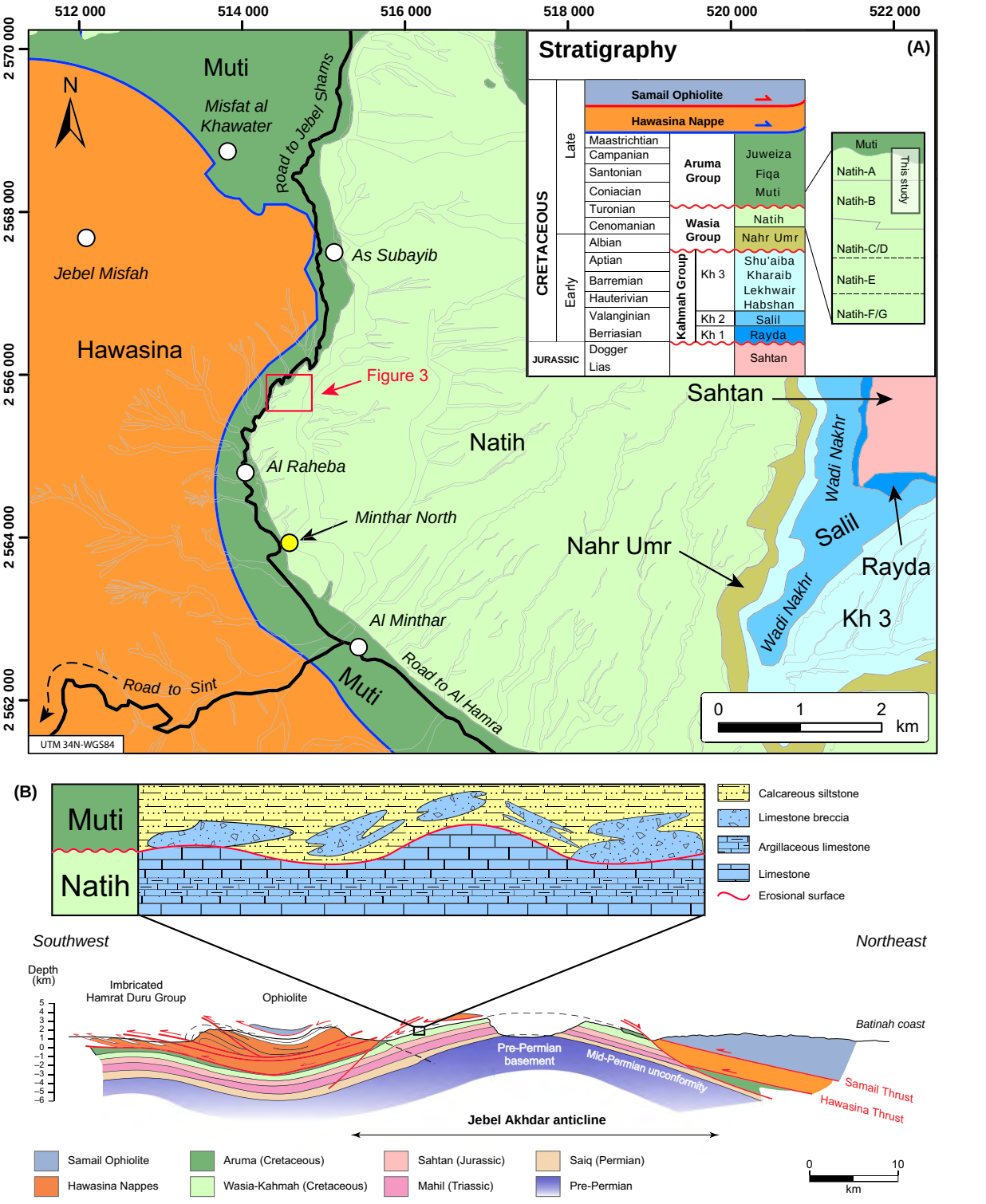

Fig. 2. (A). Geology of the southern limb of the Jebel Akhdar anticline around the Al Raheba study area. The studied outcrop comprises the topmost layers of the Natih A member of the Wasia Group. The geological map is simplified after Beurrier *et al.* (1986). The stratigraphic column is compiled from Breton *et al.* (2004), Searle (2007) and van Buchem *et al.* (2002). The map location is shown in Fig. 1. Inset summarizes the local stratigraphy. Wadis have been outlined to illustrate local topography. (B). Geological cross-section across the Jebel Akhdar anticline, modified from Searle (2007). The location of the section is indicated in Fig. 1 and illustrates the structural setting of the study area at the boundary between the Wasia Group and the Muti Formation (Aruma Group). The cross-section has no vertical exaggeration. The inset schematically illustrates the Wasia-Aruma unconformity and the heterogeneous distribution of calcareous siltstones (yellow) and limestone breccias (blue) in the Muti Formation (sketch is not to scale).

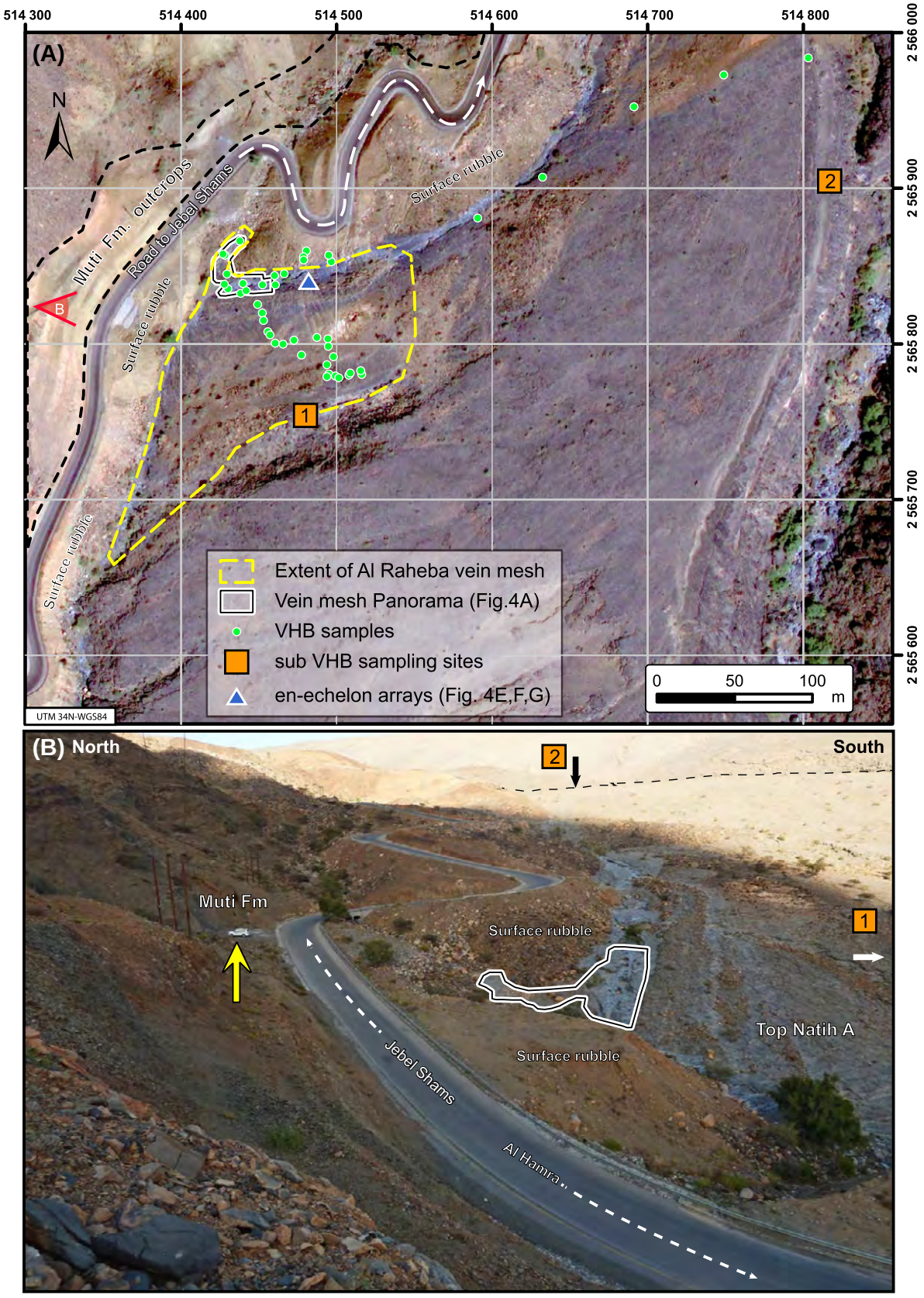
514 300
514 400
514 500
514 600
514 700
514 800
2 566 000
2 565 900
2 565 800
2 565 700
2 565 600
(A)
N
Muti Fm. outcrops
Road to Jebel Shams
Surface rubble
Surface rubble
Surface rubble
Surface rubble
B
1
2
Extent of Al Raheba vein mesh
Vein mesh Panorama (Fig.4A)
VHB samples
sub VHB sampling sites
en-echelon arrays (Fig. 4E,F,G)
0
50
100
m
UTM 34N-WGS84
(B) North
South
2
Muti Fm
Surface rubble
1
Top Natih A
Surface rubble
Jebel Shams
Al Hamra

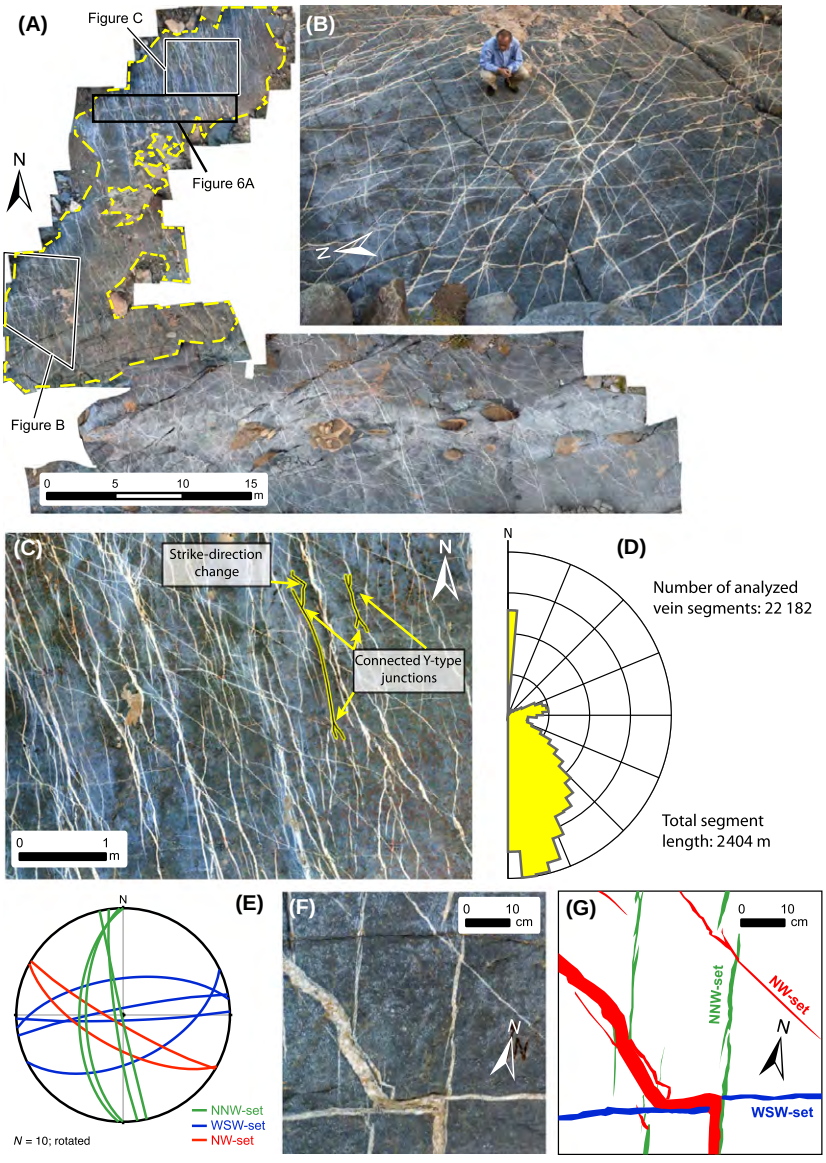

Fig. 4. Structural characterization of Stage 1 veins at outcrop scale. The average bedding orientation in the outcrop is 268/13 (dip direction/dip). (A). Panorama photograph of the investigated outcrop (map view). White calcite veins stand out clearly against gray-blue limestone. A zoomable panorama can be found at: http://www.ged.rwth-aachen.de/links/gigapixel.html. (B). Oblique view of part of the vein mesh, looking east. Note the connectivity of calcite vein segments (location is indicated in A). (C). Subset of panorama (as shown in A) in the northern part of the vein mesh. The mesh is dense and comprises several major orientation sets of vein segments. Isolated vein segments are rare, and it is difficult to track a single vein from tip to tip. (D). Rose diagram of vein segment strike orientations (normalized by length; n = 22 182; total segment length = 2404 m). The diagram is based on average orientations of vein segments that were vectorized in the northern part of the outcrop (area outlined by yellow dashed line). E. Lower hemisphere (equal area) stereoplot of veins belonging to three vein orientation sets in an area of low vein abundance adjacent to the main studied pavement area. The vein arrays occur in lateral continuity with the main vein mesh (Location indicated in Fig. 3). F. Photograph illustrating crosscutting relationships of three vein orientation sets as in figure E. (G). Sketch interpretation of F.

stress. A key conclusion was that veins at high angle to bedding formed both before and after normal faulting.

METHODS

A part of the Al Raheba vein mesh has been captured in map view as a gigapixel panorama (Figs 3 and 4). Photographs were systematically taken from an altitude of 3 m with a constant overlap using a Nikon D80. The photographs have been stitched with Autopano Giga and orthorectified in ArcGIS, based on a 2-m grid that was painted on the outcrop. Over 100 thin sections have been prepared from oriented drill plugs. The position and orientation of the thin sections were used to georeference micrographs of

Fig. 3. (A). Satellite image overview of sampling sites at the Al Raheba area. Stage 1 and Stage 2 fault veins were sampled at an outcrop comprising the three topmost layers of the Natih A member. A gigapixel panorama photograph has been created for a part of the outcrop (solid outline). The yellow dashed line indicates the approximate lateral extent of the vein mesh. The isotopic composition of the limestones, which host the vein mesh (VHB), is based on samples from locations shown as green dots. Sampling through the stratigraphy of Natih A and Natih B member limestone (below the VHB) was done at sites [1] and [2]. Stratigraphic and structural relationships with the Muti Formation above the Natih Formation are obscured by extensive surface rubble. Approximate location of en-echelon vein arrays, shown in Fig. 4, is indicated by blue triangle (GeoEye imagery, band 3, 2 and 1 as RGB, pan-sharpened; Acquisition Date: 2009-02-28). (B). Photograph of Al Raheba pavement. Location of viewing point is indicated by red eye symbol in figure A. The photograph shows the studied outcrop (solid outline) next to the road leading to Jebel Shams. On the other side of the road, about 10 m higher in the stratigraphy, yellow siltstones within the Muti Formation are exposed (at the 4WD; yellow arrow). Sites [1] and [2] as in part A of this figure.

calcite veins on the high-resolution base map provided by the gigapixel panorama. Approximate locations of vein samples and chips of proximal host rocks, whose stable isotope compositions were analyzed, were entered into the GIS system as well. Microstructures of calcite veins and stylolites were studied in transmitted and reflected light using an optical microscope. Vein structures were studied at a large range of scales (cm to μm). The orientations of tectonic stylolites oriented at high angle to bedding, were measured in the laboratory in the drill cores.

To support the microstructural investigation of stylolites, micro-Fourier Transformation Infrared Spectroscopy (μF-TIR) analyses were performed using a Perkin Elmer Spotlight 400 μFT-IR Imaging System. Image data from polished blocks (reflection mode) were collected between 4000 and 650 cm^{-1} at 16 cm^{-1} resolution with 32 scans per pixel against the gold standard. The area of the sample was imaged over 12.0 mm × 12.2 mm using a 25-μm-pixel resolution and a mirror velocity of 1 cm s^{-1}. All spectra are represented in terms of absorbance against wavelength (in cm^{-1}). Water and carbon dioxide contributed by laboratory conditions were removed by subtraction of their characteristic spectra. For data visualization, the software SPECTRUM IMAGE was used.

At outcrop scale, 182 crosscutting relationships between intersecting veins were logged. The relationship was determined by (i) structural superposition (intersection relationships, i.e., dextral or sinistral strike separation), or (ii) clearly different vein cement colors (cf. Holland *et al.* 2009a).

In a subset of the gigapixel panorama (Fig. 4A), vein intersection points, vein tips, and connecting vein segments were vectorized. This created a dataset of about 8500 intersection points, 10 000 vein tips, and 16 000 vein segments. The average strike orientation of each vein segment was calculated using the long axis of the minimum bounding geometry (MBG rectangle by area; Esri 2012). These data were used to analyze strike orientation, length, and frequencies of vein segments (Fig. 4D).

Carbon and oxygen isotope composition has been analyzed in 166 calcite samples. Eighty-seven samples were from calcite veins, 15 samples were from limestone host rock <5 mm from vein margins ('proximal' host rock samples), 48 samples were from limestone host rock remote from veins ('distal' host rock samples, >30 cm from visible vein development), and 16 samples were from limestone within the Natih A and Natih B members up to 50 m below the vein-hosting limestone beds (VHB) near the top of the Natih A member. Calcite and limestone were all sampled from clean and unweathered material, away from ground surface dissolution effects and surficial deposits of calcite flowstone.

Calcite samples selected for analysis were typically <1–2 mm^3 in volume. These were crushed and ~200 μg of powder was separated for analysis. The measurements were made at the Australian National University, Research School of Earth Sciences, using a Finnigan MAT 251 mass spectrometer with a Kiel microcarbonate device using 105% phosphoric acid dissolution at 90°C for 12 min. NBS-19 and NBS-18 standards were analyzed after every 8 samples. C/O isotopic composition was normalized to the NBS-19 standard having $\delta^{18}O_{VPDB} = -1.41$ ‰ and $\delta^{13}C_{VPDB} = 1.95$ ‰. The $\delta^{18}O_{VPDB}$ composition was converted to VSMOW using the relationship

$$\delta^{18}O_{VSMOW} = 1.03091(\delta^{18}O_{VPDB}) + 30.09.$$

The external precision (1σ standard deviation) for isotopic analyses of calcite was typically <0.06 ‰ for $\delta^{18}O$ and <0.04 ‰ for $\delta^{13}C$. This is estimated from results for the NBS-19 and NBS-18 standards run concurrently.

RESULTS

Structures at meso- and microscale

Description of the vein mesh

The studied limestone outcrop is close to the village Al Raheba, next to the road leading to Jebel Shams. It comprises a bedding-parallel pavement, which exposes a mesh of calcite veins in the three topmost layers of the Natih A member (see Figs 1–3; 514433 mE 2565865mN UTM 40N). The location has been mentioned by Holland *et al.* (2009b), (their figure 8e,f) and the vein mesh has been described by Virgo & Arndt (2010).

The vein mesh is confined to three exposed limestone beds, which occur at the top of the Natih A member (referred to as VHB, vein-hosting beds) with a total thickness of 3.5 m, immediately below the contact with the Muti Formation. The bedding dips gently westward (268/13; dip direction/dip). The three layers of the VHB are exposed over approximately 2.4×10^5 square meters and contain varying densities of steeply dipping calcite veins with various strike orientations. The vein mesh at Al Raheba (outlined in Fig. 3) covers an area of at least 2000 square meters and represents the highest density in the pavement study area (Figs 3 and 4). The density of veins in the VHB decreases away from this outcrop. The limits of the Al Raheba vein mesh to the west and north are not known due to lack of outcrop at the stratigraphic level of the VHB. Holland *et al.* (2009a) described high-density vein networks as being proximal to faults. The vein mesh at Al Raheba is approximately 1.2 km away from the closest fault on the map of Holland *et al.* (2009b). Satellite image interpretation and direct field observations in the area confirm that there are no substantial faults (displacement >10 cm) associated with the Al Raheba vein mesh.

Figure 4 shows an overview panorama of the outcrop. The white calcite veins stand out clearly from the gray lime-

stone in the polished outcrop. Individual veins are up to 3 cm wide. The vein mesh is highly interconnected in this outcrop; it is difficult to find individual veins that do not intersect others. Therefore, attempting to measure the 'standard' vein or fracture geometries (i.e., length, aspect ratios; cf. Vermilye & Scholz 1995) is not meaningful. Below the resolution of the photographs (1 mm), a multitude of microveins can be seen with hand lens and in thin section. Microveins are present in every sample examined so far, with widths down to the resolution of the optical microscope.

The vein mesh at Al Raheba is interpreted to comprise two generations of veins. Detailed study of crosscutting relationships between veins at outcrop scale (see Holland *et al.* 2009a) indicates that most vein intersections do not have clear or consistent relative age relationships. Clear crosscutting relationships were observed only for a single E-W-striking, dilatant, calcite-filled normal fault. Veins in this normal fault are termed Stage 2 fault veins. All older veins are classified as Stage 1 veins.

Adjacent to the main pavement (Figs 3 and 4A), the vein mesh is less dense and three distinct orientation sets of extension veins have consistent crosscutting relationships (Fig. 4E,F,G). The oldest set comprises N-S-striking veins; these are crosscut by E-W-striking veins of an intermediate age set. The youngest vein set is NW-SE-striking and partly reactivates veins of the previous vein sets (Fig. 4F, G). Such consistent age relationships are not present in the main outcrop (see below).

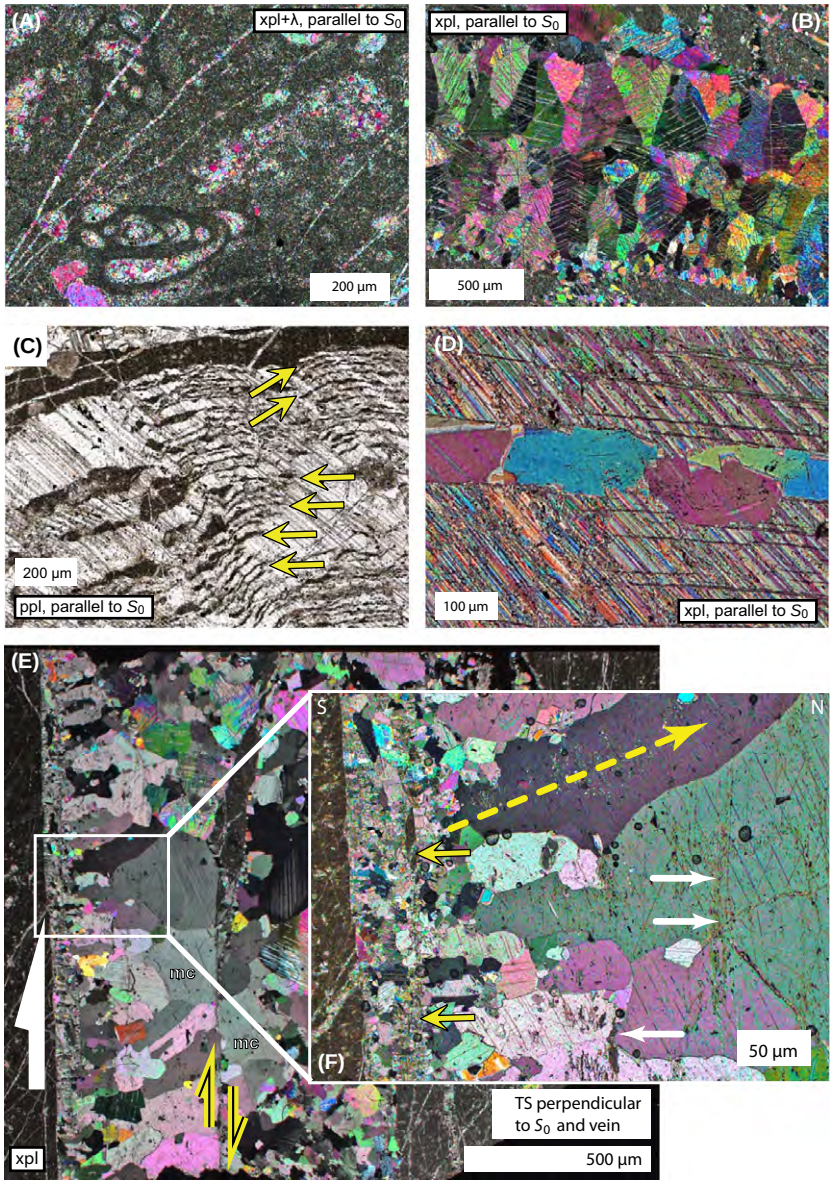

Fig. 5. (A). Micrograph of the fine-grained, matrix-supported limestone host rock with abundant benthic foraminifera and several microveins. Cross-polarized light (xpl) with gypsum plate (λ) inserted. Section is parallel to bedding (S_0). (B). Elongate-blocky microfabric of a Stage 1 vein with a clearly visible median zone near the center of the vein. (C). Swarms of host rock inclusion bands (yellow arrows) that are oriented parallel to the vein walls are common in Stage 1 veins and indicate antitaxial vein growth. (D). A microvein within a Stage 1 calcite vein; note that the coarse early calcite has closely spaced mechanical twins, whereas calcite in the late microvein contains few mechanical twins. (E). Microstructural overview of a Stage 2 fault vein. The thin section (TS) is perpendicular to both bedding and the vein (see Fig. 6D,E for location). The vein is composed of two clearly distinguishable subdomains, which are of similar width (400 µm). The hanging wall part (N side) has a blocky texture with variable grain size and abundant mechanical twinning. In the footwall part, calcite grain size increases toward the vein center and mechanical twins are less abundant. Offset of single marker crystal grains (mc) is identified across the median boundary. This indicates that the hanging wall part has been displaced here about 200 µm in dip-slip direction. (F). Detailed view of footwall part of the fault vein. The vein rim is characterized by a zone, up to 60 µm wide, composed of blocky calcite with small grain size. A thin, discontinuous, host rock inclusion band (solid, yellow arrows) occurs approximately 50 µm from the vein margin. Toward the center, an elongate-blocky fabric has a slight preferred shape orientation (SPO). A yellow dashed arrow highlights the SPO, as well as the inferred crystal growth direction. Note: Large calcite crystals locally contain host rock inclusion bands, which are parallel to the vein boundary (white arrows).

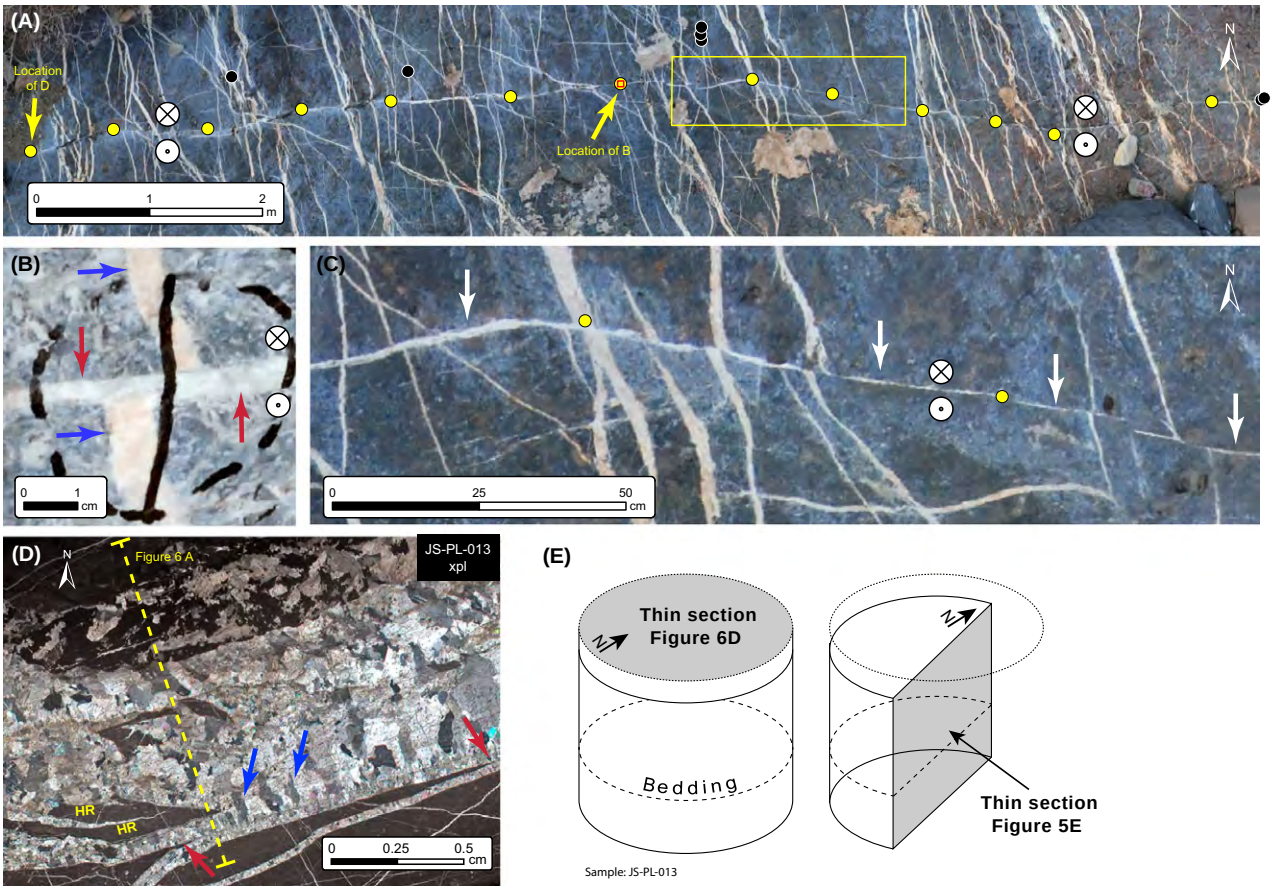

Fig. 6. Structures of the late normal fault (Stage 2). (A). Panoramic overview of the Stage 2 normal fault (Location indicated in Fig. 4A). Locations of fault vein samples are marked by circles (Stage 1 in black; Stage 2 in yellow). (B). A close-up view of a Stage 1 vein (blue arrows) that is clearly offset by the Stage 2 fault vein (red arrows). (C). Detail of A illustrating the systematic structural superposition of the normal fault (white arrows) against veins of Stage 1. The location of the image is indicated by the yellow box in A. (D). Microstructural overview of a Stage 2 fault vein (crossed polarized light; thin section parallel to bedding; location indicated in A). The yellow dashed line indicates the location of a thin section perpendicular to both bedding and to the fault vein (see Fig. 5E,F). The central part of the vein is characterized by blocky calcite cements. On the lower rim of the vein host rock inclusions are present (HR), as well as thin veins that branch from the thick vein (red arrows). These thin, branching veins contain fine-grained calcite. Where they merge with the main vein, they form fine-grained marginal zones in the main fault vein (Fig. 5F). Elongate-blocky crystals across textural boundaries in the vein indicate epitaxial crystal growth (blue arrows). E. Sketch illustrating orientation of thin sections in Figs 6D and 5E respectively.

Stage 1 veins

Stage 1 veins form a complex mesh of calcite veins at high angle to bedding containing three dominant orientation populations that correspond broadly to those present outside the main outcrop. The most abundant orientation set of veins trend NNW-SSE. The second most abundant set strikes NW-SE, and the least common orientation set has a WSW-ENE strike direction (Fig. 4). The mesh formed by Stage 1 veins is characterized by a range of different types of junctions of vein segments (X-, Y-, and T-type junctions). The vast majority of junctions show no shear offset. In this vein mesh, complex and often mutually crosscutting relationships are common (e.g., two veins in an X-type intersection, with the first orientation crosscut by a second at one locality, which in turn is crosscut by the first orientation at an adjacent locality). At the thin section scale, similar mutually inconsistent relationships occur within one vein junction.

Thicker veins commonly have horsetail-type splays developed near their terminations. Bundles of anastomosing veins are common, together with stacked veins (one thicker segment connecting two veins in a Y-type junction; cf. Virgo *et al.* 2013a). En-echelon arrays of shorter veins are present in places. In some cases, veins change their orientation by up to 90°, without a corresponding junction (Fig. 4C).

At the microscale, the host rock limestone is a wackestone with a fine-grained micritic matrix and fossil

fragments. Sparitic cement fills of fossils are always overprinted by microveins (Fig. 5A). In thicker veins, calcite is coarse-grained and blocky. In thin veins (e.g., typically <1 mm thick), elongate-blocky microstructures are common. Growth competition is indicated in places by a progressive increase in grain size from host rock toward the vein center where, in some cases, a median line is present (Fig. 5B). At microscale, regularly spaced host rock inclusions are commonly developed in single large calcite crystals; these bands of inclusions are parallel to the vein–rock interface (Fig. 5C); these structures are evidence for antitaxial crack-seal growth (cf. Ramsay 1980; Holland & Urai 2010). The spacing of host rock inclusion bands ranges between 4 and 40 μm. The spacing of crack-seal inclusion bands indicates that formation of a 1-cm-thick vein involves between 2500 (4 μm spacing) and 250 (40 μm spacing) crack-seal events. The majority of vein calcite crystals are mechanically twinned, indicating minor deformation after crystallization (Fig. 5B,D).

In many thin sections, a combination of different microstructures was present, which can be classified using the terminology of Holland & Urai (2010): Case 1 (microveins forming in the preexisting vein; Fig. 5D), Case 2 (solitary microveins form in the adjacent host rock; Fig. 5A), Case 4 (rough reactivation of vein–host rock interface and inclusion of host rock material; Fig. 5C), and Case 5 (sharp reactivation of vein–host rock interface without inclusion of host rock material; Fig. 5C).

Stage 2 veins

The second generation of vein formation is represented by a single E-W-trending, partly dilatant, calcite-filled normal fault. This fault consistently crosscuts the Stage 1 veins and dips northwards at about 65° relative to the bedding. It has a total length of 10 m, a maximum width of 2 cm, and a maximum dip separation of 10 cm. At its eastern end, the fault splits into two strands (Fig. 6). The dilatant, calcite-filled parts of the faults are referred to as Stage 2 fault veins. On the basis of its length and dip separation, this normal fault could penetrate to a depth of order 10 m below the VHB (Walsh *et al.* 2003; Kim & Sanderson 2005). In thin section, Stage 2 calcite has blocky to elongate blocky fabrics. Some large crystals (>8 mm) contain less mechanical twinning than calcite in Stage 1 veins (Fig. 5E,F). Observations made perpendicular to the vein and parallel to the dip-slip direction indicate that the Stage 2 veins contain evidence for both shear reactivation and dilation. Elongate crystal shapes and offsets between the vein wall and host rock inclusion bands indicate opening at high angles to the vein wall (Fig. 5E,F). In contrast, very narrow shear planes offset marker crystals with the same crystallographic orientation (Fig. 5E).

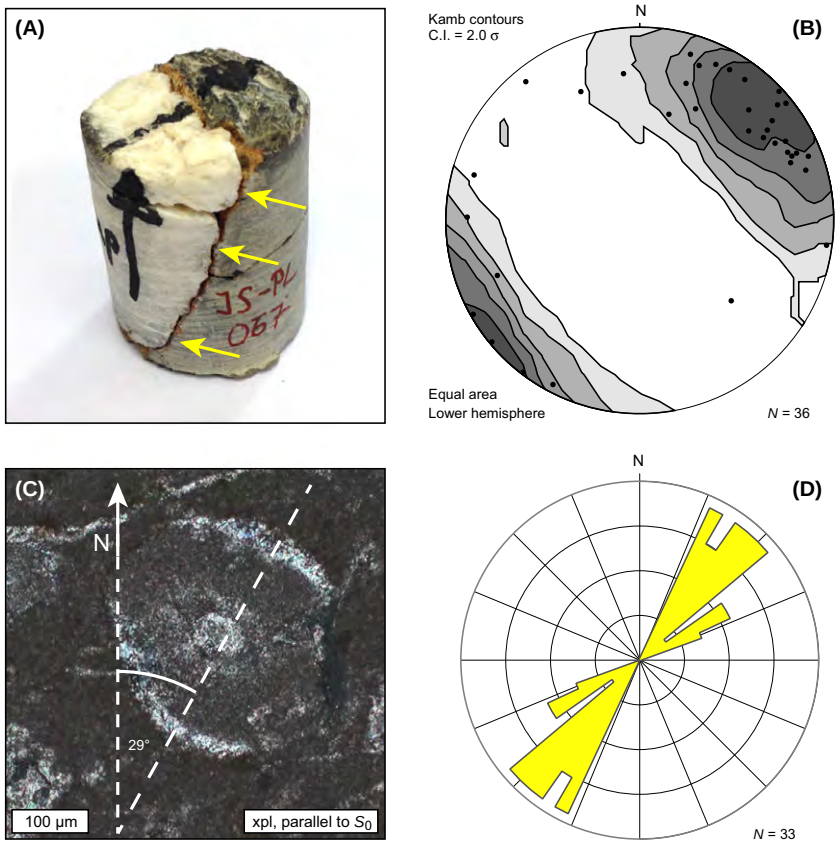

Fig. 7. (A). Core sample showing a stylolite at high angle to bedding (tectonic stylolite) that has partly dissolved a NW-SE-striking calcite vein (yellow arrows). The top plane of the sample is parallel to bedding (top black arrow points to N). (B). Equal area, lower hemisphere stereoplot of poles to tectonic stylolite orientations with contours after Kamb (1959). The stylolites show a predominant steeply SW-dipping orientation. (C). Quartz-strain fringe around a quartz-bearing fossil. The fringes contain mostly elongated, fibrous quartz crystals with a well-developed shape preferred orientation. The long axis of the strain shadow is indicated by white dashed line. (D). Rose diagram of quartz-strain fringe strike orientations. The lineations are predominantly trending NE-SW.

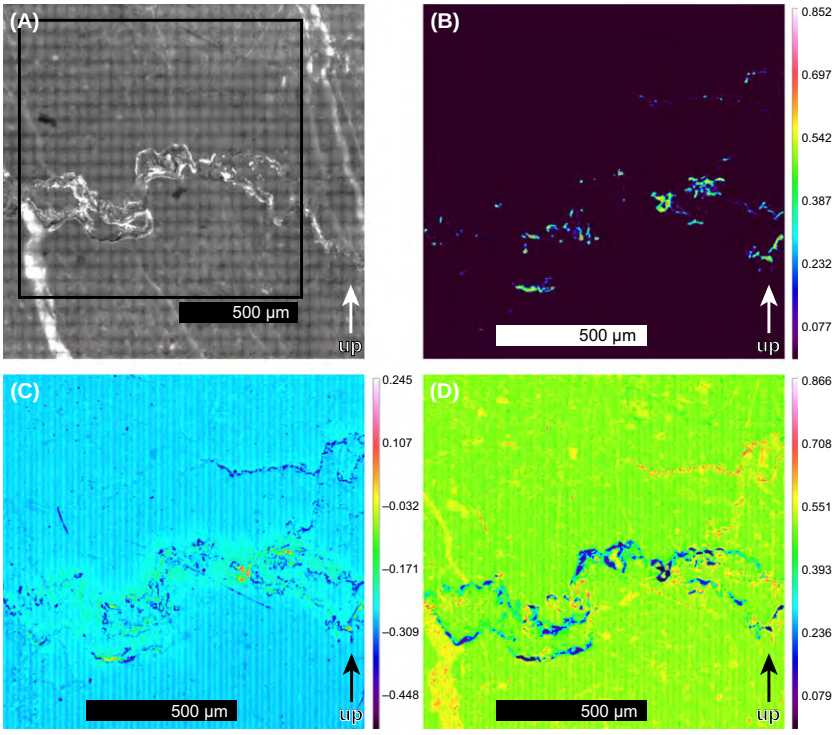

Fig. 8. (A). Reflected light micrograph of a polished VHB limestone block containing bedding-parallel stylolites. The polished surface is perpendicular to the bedding. The stratigraphic location is at the boundary between the lowermost and middle layer of the VHB. White reflections in the stylolite indicate presence of quartz. (B). µFT-IR average absorption map of a bedding-parallel stylolite. The analyzed area is indicated in Fig. 8A. Green and blue colors indicate presence of organic matter located at the stylolite. The limestone matrix shows up in black. Color bar represents absorbance versus wavelength (in cm^{-1}). (C). Band-pass filter µFT-IR absorption map showing the relative distribution of aromatic compounds. Yellow and red colors indicate relative high amounts. Note the halo around the stylolite that can be distinguished from the limestone matrix (in cyan color). Color bar represents absorbance versus wavelength (in cm^{-1}). (D). Band-pass filter µFT-IR absorption map showing the relative distribution of aliphatic compounds. Yellow and red colors indicate relatively high amounts. The map reveals the presence of a thin stylolite above the main stylolite as shown by red colors. The limestone matrix shows up in green colors. Color bar represents absorbance versus wavelength (in cm^{-1}).

Other deformation features

Both burial and tectonic stylolites are abundant in the VHB at macroscopic and microscopic scale. At macroscale, bedding-parallel stylolites (i.e., burial stylolites) are generally crosscut by Stage 1 veins. Tectonic stylolites are at a high angle to bedding and commonly crosscut NNW-SSE-striking Stage 1 veins (Fig. 7A). However, the stylolites are crosscut by some NW-SE and WSW-ENE-striking Stage 1 veins. The majority of the tectonic stylolites dip steeply SW (Fig. 7B). Relatively insoluble material, such as detrital quartz and organic matter, has been enriched in stylolites. Aliphatic and aromatic compounds are enriched in the stylolites as shown by the µFT-IR analysis (Fig. 8). Organic matter is typically so fine-grained that individual grains commonly cannot be resolved using optical microscopy.

Strain fringes are present around spheroidal, quartz-bearing fossils, as well as around quartz accumulations at stylolites (Fig. 7C). The fringes contain elongate to fibrous quartz which defines a shape preferred orientation (SPO). Both the SPO and the long axes of the fringes are bedding parallel and trend NE-SW (Fig. 7D).

Veins above and below the vein-hosting beds

The layers immediately below the VHB contain no macroscopic veins. The next thick limestone layer 10 m below the VHB contains two sets of widely spaced (5 m) calcite veins that are up to 5 cm thick. These are at a high angle to bedding and strike NW-SE, parallel to the NW set of Stage 1 veins (cf. Fig. 4E,F,G). These veins are clearly visible in satellite images (Holland *et al.* 2009a) and are consistently crosscut by a less prominent WSW-striking set of veins.

In the Muti Formation directly overlying the VHB in our study area, there is no exposure. About 10 m higher in the Muti Formation, there is very limited vein development. In outcrops close by (1 km to north), especially in carbonate breccias which are locally in direct contact with the Natih Formation, there are many calcite veins. Detailed study of the veins in the Muti is the subject of a follow-up project. However, initial interpretations indicate that the

geometry of these veins is not simply related to those of veins in the Natih Formation.

C and O isotopic compositions

Host rocks

Vein-hosting beds (VHB)

Samples of distal host rock in the VHB were taken more than 30 cm away from any visible vein. Two lateral sampling traverses were used to characterize variations of C/O isotopic composition of limestone in the VHB. One traverse extends more than 400 m to NE, and the other was 200 m long in an EW trend from the center of the vein mesh (Fig. 3A). The $\delta^{18}O$ composition of the limestone host rock in the VHB ranges from 21.8‰ to 23.7 ‰; the $\delta^{13}C$ composition ranges from 1.5‰ to 2.3 ‰. C/O stable isotope compositional ranges of the VHB are shown in Fig. 9, while in Fig. 10 both C and O isotopic composition are plotted against their stratigraphic depth The entire suite of C/O stable isotope compositions are presented in Table 1.

Natih A and B members beneath the VHB

The Natih A and B members were sampled along vertical traverses in nearby wadis (Fig. 3) to characterize the variation in C/O isotopic composition over a ~50 m stratigraphic interval beneath the VHB. Toward the top of the Natih A member, the limestones become ^{18}O-depleted relative to those at deeper stratigraphic levels (Fig. 10). The highest $\delta^{18}O$ values are found in sequence III-4 of the Natih B member and in a narrow excursion about 5 m below the VHB. From 50 m beneath the VHB, there is a progressive decrease in $\delta^{18}O$ from 25 ‰ to approximately 24 ‰ toward the hard ground limestone layer 10 m below. Within the overlying nodular facies limestones, there is a progressive upwards increase in $\delta^{18}O$ until 5 m below the VHB. From this narrow positive excursion upward in the stratigraphy, there is a progressive decrease in $\delta^{18}O$ upward in the stratigraphy, with the lowest values in the sequence occurring within the VHB.

The cliff-building limestones between 10 m and 30 m below the VHB are enriched in ^{13}C relative to the rest of the sequence. The $\delta^{13}C$ composition of sequence III-4 within the Natih B member is comparable to the $\delta^{13}C$ composition in the VHB (Fig. 10). The $\delta^{18}O$ and $\delta^{13}C$ composition of the VHB is up to 7 ‰ lower and up to 1 ‰ higher, respectively, than typical Upper Cretaceous (94–91 Ma for Natih A member) marine limestones (cf. Veizer *et al.* 1999).

Proximal host rock

Proximal host rock samples have been taken within a few mm of Stage 1 and Stage 2 veins. The range for $\delta^{18}O$ in the proximal limestone is from 22.5–23.7 ‰. The range for $\delta^{13}C$ is between 1.1 and 1.9 ‰. This compositional range is narrower than the range for distal VHB isotopic

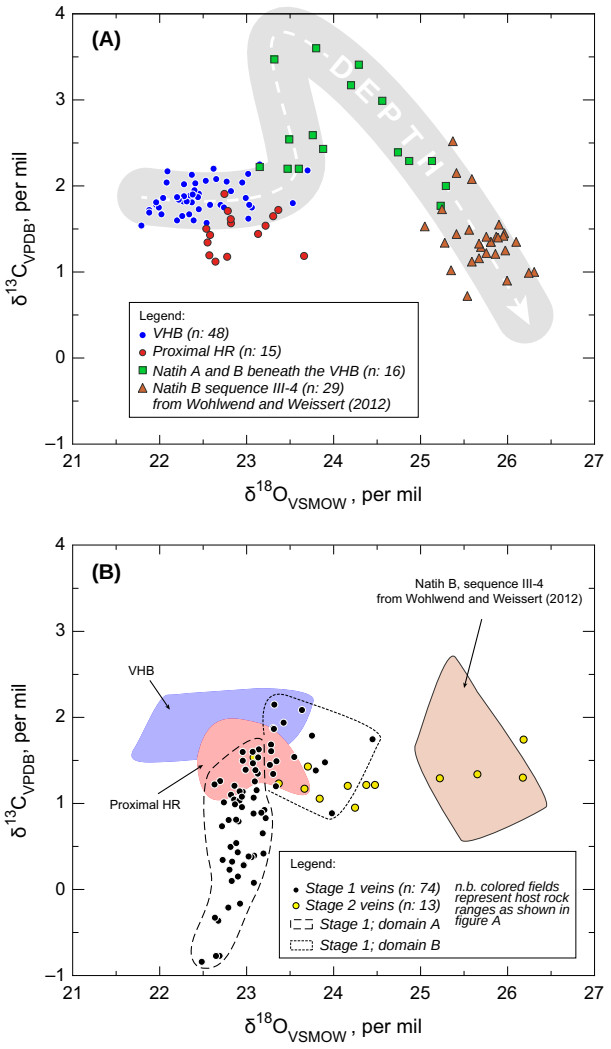

Fig. 9. (A). Stable isotope composition of limestones in members A and B of the Natih Formation. The blue dots represent samples from the vein-hosting beds (VHB). These samples have been taken at least 30 cm away from visible calcite veins. The red dots show the isotopic composition of limestone host rocks immediately adjacent to Stage 1 and Stage 2 fault veins within the VHB. Isotopic composition of limestone layers below the VHB is indicated by green squares. The brown triangles show isotopic composition of limestones within sequence III-4 of the B member of the Natih Formation (data from Wohlwend & Weissert 2012). (B). Carbon and oxygen isotope composition of vein calcites (hosted by VHB) compared with the isotopic compositional ranges of limestone in the local stratigraphy. The ranges of C/O isotopic composition of limestones (from Fig. 9A) are indicated as follows: Blue – VHB; red – proximal host rocks within VHB; brown – Natih B member. For Stage 1 veins (black dots), two domains (A and B) are defined. Domain A has a narrow range for $\delta^{18}O$, and A shows a marked variation in $\delta^{13}C$ values. The C/O isotopic composition of veins within domain B is generally enriched in ^{18}O relative to domain A, but have a $\delta^{13}C$ composition similar to the VHB. Stage 2 fault veins are indicated by yellow circles.

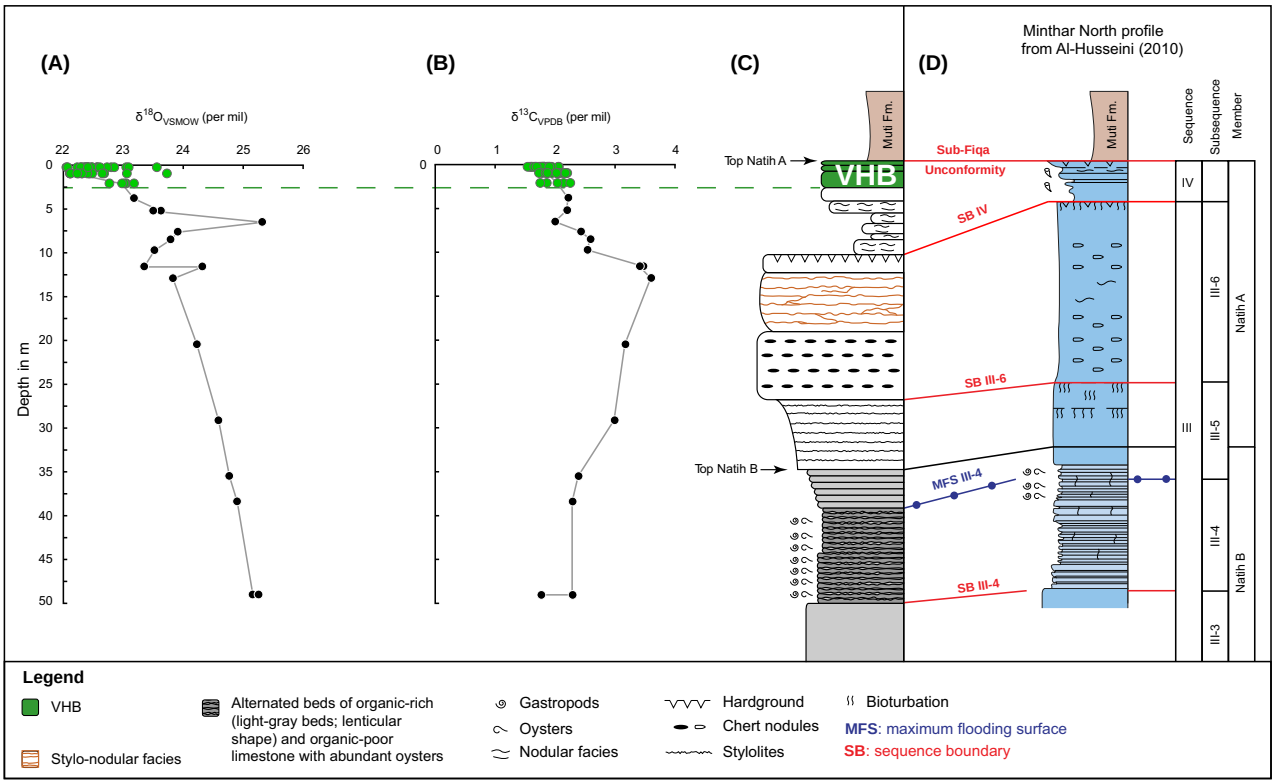

Fig. 10. Variations in $\delta^{18}O$ (A) and $\delta^{13}C$ (B) in distal limestones as a function of depth beneath the top of the VHB. The local stratigraphy at the Al Raheba site is shown in (C). The regionally developed sequence stratigraphy within the Natih A member and the top of Natih B member at Minthar north (1.8 km south of the study area) is illustrated in D (after Al-Husseini, 2010). Note a clear trend of decreasing $\delta^{18}O$ and $\delta^{13}C$ compositions toward the top of the Natih A member. Yellow siltstones from the overlying Muti Formation did not contain enough carbonate to obtain C/O isotope ratios. The contact between the Natih Formation and the Muti Formation is not exposed at Al Raheba.

compositions. The $\delta^{18}O$ range is at the higher end of the range found in the distal host rock (VHB) (Fig. 9A). Significantly, approximately 50% of the proximal host rock samples have $\delta^{13}C$ values up to 0.5 ‰ lower than the $\delta^{13}C$ compositional range of the distal VHB (Fig. 9A).

Vein calcite

Stage 1 veins

The $\delta^{18}O$ composition of Stage 1 vein calcite varies from 22.5 ‰ to 24.4 ‰, while $\delta^{13}C$ composition ranges from −0.8 ‰ to 2.1 ‰ (Fig. 9B). For $\delta^{13}C$ <0.8 ‰, there is little variation in $\delta^{18}O$ composition (22.5–23.2 ‰). Above a $\delta^{13}C$ value of 0.8 ‰, there is a wider spread in $\delta^{18}O$ values with a maximum of 24.4 ‰ (Fig. 9B). Accordingly, we distinguish two compositional domains (A and B) within Stage 1 veins. Domain A veins have $\delta^{18}O$ <23.3 ‰. This is within the $\delta^{18}O$ compositional range of the VHB. A few Stage 1 veins are ^{18}O-enriched relative to the VHB by up to 0.7 ‰ and define domain B (Fig. 9B). The domain B veins are characterized by a more restricted variation in $\delta^{13}C$ (0.9–2.1 ‰) than domain A composition (−0.8–1.6 ‰) (Fig. 9B). There is no obvious relationship between vein orientation and $\delta^{18}O$ composition of vein calcite. Importantly, domain B veins (i.e., with $\delta^{18}O$ >23.3 ‰) are not restricted to any particular orientation set of Stage 1 veins (Fig. 11). Additionally, Domain B veins all occur in the lowermost of the three VHB beds and have no spatial association with the Stage 2 fault. In general, domain 1B veins tend to be the youngest veins in thin section and crosscut domain 1A veins.

Stage 2 fault veins

Vein calcite in the Stage 2 fault veins has a very narrow range in $\delta^{13}C$ (1.0–1.7 ‰), whereas $\delta^{18}O$ ranges from 23.1 to 26.2 ‰. The $\delta^{18}O$ compositions of Stage 2 calcite are evenly distributed between the minimum and the maximum value. Significantly, the minimum $\delta^{18}O$ value of Stage 2 calcite is 1.6 ‰ higher than the minimum $\delta^{18}O$ value of the VHB (Fig. 9B). Furthermore, the average $\delta^{13}C$ value (1.3 ‰) is 0.6 ‰ lower than the average $\delta^{13}C$ value of the VHB (Fig. 9B).

Isotopic variations within veins

Although the analyzed population of Stage 1 veins has a restricted range of oxygen isotope compositions, within veins there can be up to 2 ‰ variation in $\delta^{13}C$ between

Table 1 Veins and limestone compositions within the vein-hosting beds

Sample-id	δ^{18} OVSMOW ‰	δ^{13} CVPDB ‰	Description
2-2009	23.2	0.9	Stage 1 vein calcite
4-2009	23.1	0.4	Stage 1 vein calcite
5-2009	22.8	1.1	Stage 1 vein calcite
7-2009	22.8	0.5	Stage 1 vein calcite
8-2009	23.2	0.4	Stage 1 vein calcite
11-2009	22.7	−0.4	Stage 1 vein calcite
13-2009	22.8	0.8	Stage 1 vein calcite
15-2009	23.1	1.6	Stage 1 vein calcite
16-2009	23.8	1.4	Stage 1 vein calcite
17-2009	23.1	1.6	Stage 1 vein calcite
18-2009	23.0	1.6	Stage 1 vein calcite
19-2009	23.0	1.5	Stage 1 vein calcite
20-2009	23.1	1.5	Stage 1 vein calcite
25-2009	22.9	0.5	Stage 1 vein calcite
27-2009	22.8	−0.2	Stage 1 vein calcite
35-2009	23.3	1.7	Stage 1 vein calcite
36-2009	23.5	1.5	Stage 1 vein calcite
37-2009	23.3	1.6	Stage 1 vein calcite
38-2009	23.1	0.4	Stage 1 vein calcite
46-2009	23.0	1.4	Stage 1 vein calcite
49-2009	23.2	0.7	Stage 1 vein calcite
54-2009	23.1	1.3	Stage 1 vein calcite
59-2009	24.4	1.7	Stage 1 vein calcite
63-2009	26.2	1.3	Stage 2 vein calcite
65-2009	24.2	1.2	Stage 2 vein calcite
68-2009	32.0	−4.8	Stage 2 vein calcite
70-2009	25.2	1.3	Stage 2 vein calcite
72-2009	23.4	1.2	Stage 2 vein calcite
74-2009	26.2	1.7	Stage 2 vein calcite
76-2009	23.1	1.5	Stage 2 vein calcite
77-2009	25.7	1.3	Stage 2 vein calcite
79-2009	23.7	1.4	Stage 2 vein calcite
84-2009	24.5	1.2	Stage 2 vein calcite
88-2009	23.3	1.3	Stage 2 vein calcite
90-2009	23.8	1.1	Stage 2 vein calcite
91-2009	24.4	1.2	Stage 2 vein calcite
92-2009	23.7	1.2	Stage 2 vein calcite
94-2009	24.2	1.0	Stage 2 vein calcite
97-2009	22.9	1.0	Stage 1 vein calcite
98-2009	22.9	1.0	Stage 1 vein calcite
99-2009	22.7	1.0	Stage 1 vein calcite
105-2009	22.9	1.0	Stage 1 vein calcite
110-2009	22.9	1.2	Stage 1 vein calcite
111-2009	22.9	0.8	Stage 1 vein calcite
117-2009	23.1	1.5	Stage 1 vein calcite
124-2009	22.9	0.8	Stage 1 vein calcite
125-2009	22.9	1.1	Stage 1 vein calcite
126-2009	23.0	1.1	Stage 1 vein calcite
127-2009	23.3	1.5	Stage 1 vein calcite
128-2009	23.1	1.4	Stage 1 vein calcite
132-2009	24.0	0.9	Stage 1 vein calcite
133-2009	23.1	1.3	Stage 1 vein calcite
135-2009	23.9	1.5	Stage 1 vein calcite
137-2009	23.0	0.4	Stage 1 vein calcite
141-2009	23.8	1.8	Stage 1 vein calcite
144-2009	22.9	1.1	Stage 1 vein calcite
145-2009	22.8	0.3	Stage 1 vein calcite
148-2009	22.8	0.1	Stage 1 vein calcite
149-2009	23.3	1.9	Stage 1 vein calcite
151-2009	23.1	0.1	Stage 1 vein calcite
152-2009	23.2	0.8	Stage 1 vein calcite
153-2009	22.6	−0.3	Stage 1 vein calcite
156-2009	22.9	−0.2	Stage 1 vein calcite
158-2009	23.0	0.3	Stage 1 vein calcite
161-2009	23.1	1.2	Stage 1 vein calcite

Table 1. (Continued)

Sample-id	δ^{18} OVSMOW ‰	δ^{13} CVPDB ‰	Description
162-2009	22.9	1.1	Stage 1 vein calcite
165-2009	22.8	0.2	Stage 1 vein calcite
167-2009	22.7	0.3	Stage 1 vein calcite
168-2009	23.2	0.9	Stage 1 vein calcite
169-2009	23.4	1.9	Stage 1 vein calcite
170-2009	23.6	2.1	Stage 1 vein calcite
171-2009	23.3	1.2	Stage 1 vein calcite
175-2009	23.3	1.9	Stage 1 vein calcite
180-2009	23.0	1.4	Stage 1 vein calcite
181-2009	23.3	1.4	Stage 1 vein calcite
183-2009	22.7	1.3	Stage 1 vein calcite
187-2009	22.5	−0.8	Stage 1 vein calcite
189-2009	22.6	1.2	Stage 1 vein calcite
193-2009	22.7	0.7	Stage 1 vein calcite
195-2009	22.9	0.4	Stage 1 vein calcite
196-2009	22.7	−0.8	Stage 1 vein calcite
198-2009	22.6	−0.8	Stage 1 vein calcite
199-2009	23.0	0.3	Stage 1 vein calcite
201-2009	23.1	1.1	Stage 1 vein calcite
202-2009	23.1	0.9	Stage 1 vein calcite
205-2009	22.9	1.0	Stage 1 vein calcite
206-2009	22.9	0.2	Stage 1 vein calcite
208-2009	23.3	2.1	Stage 1 vein calcite
29-2009	23.2	1.5	Proximal host rock
47-2009	22.7	1.9	Proximal host rock
52-2009	23.3	1.6	Proximal host rock
66-2009	22.8	1.6	Proximal host rock
95-2009	22.6	1.3	Proximal host rock
101-2009	22.6	1.4	Proximal host rock
106-2009	22.6	1.1	Proximal host rock
112-2009	22.6	1.2	Proximal host rock
114-2009	22.8	1.7	Proximal host rock
118-2009	22.8	1.6	Proximal host rock
122-2009	22.5	1.5	Proximal host rock
140-2009	23.1	1.4	Proximal host rock
154-2009	23.7	1.2	Proximal host rock
174-2009	23.4	1.7	Proximal host rock
185-2009	22.8	1.2	Proximal host rock
25-2012	22.2	1.6	Distal host rock
49-2012	22.27	1.82	Distal host rock
54-2012	22.37	1.81	Distal host rock
52-2012	22.53	2.06	Distal host rock
51-2012	22.77	2.05	Distal host rock
53-2012	23.02	1.62	Distal host rock
36-2012	23.53	1.8	Distal host rock
23-2012	22.54	1.57	Distal host rock
24-2012	23.06	1.75	Distal host rock
26-2012	22.34	1.67	Distal host rock
28-2012	21.96	1.78	Distal host rock
29-2012	22.02	1.67	Distal host rock
30-2012	22.04	1.86	Distal host rock
31-2012	21.99	1.75	Distal host rock
33-2012	22.39	1.6	Distal host rock
34-2012	21.79	1.54	Distal host rock
35-2012	21.96	1.81	Distal host rock
39-2012	22.45	1.91	Distal host rock
40-2012	22.31	1.82	Distal host rock
43-2012	22.44	1.87	Distal host rock
45-2012	22.35	1.89	Distal host rock
46-2012	22.26	1.65	Distal host rock
2-2012	22.82	1.94	Distal host rock
4-2012	22.7	1.78	Distal host rock
7-2012	21.88	1.72	Distal host rock
11-2012	22.58	1.78	Distal host rock

Table 1. (Continued)

Sample-id	$\delta^{18}O_{VSMOW}$ ‰	$\delta^{13}C_{VPDB}$ ‰	Description
12-2012	21.88	1.69	Distal host rock
56-2012	23.7	2.18	Distal host rock
27-2012	23.03	1.78	Distal host rock
50-2012	22.41	2.03	Distal host rock
55-2012	22.65	2.08	Distal host rock
32-2012	22.28	1.88	Distal host rock
37-2012	22.62	2.2	Distal host rock
38-2012	22.4	1.95	Distal host rock
41-2012	22.08	2.04	Distal host rock
42-2012	22.45	1.73	Distal host rock
44-2012	22.37	2.13	Distal host rock
47-2012	22.08	2.04	Distal host rock
1-2012	22.09	2.17	Distal host rock
5-2012	22.22	1.84	Distal host rock
8-2012	22.28	2.02	Distal host rock
48-2012	23.018	2.14	Distal host rock
3-2012	22.99	1.86	Distal host rock
6-2012	23.15	2.25	Distal host rock
9-2012	22.74	1.75	Distal host rock

Limestone compositions below the vein-hosting beds

Sample-id	$\delta^{18}O_{VSMOW}$ ‰	$\delta^{13}C_{VPDB}$ ‰	Depth (m)	Description
13-2012	22.4	1.9	0.3	Natih A
14-2012	22.2	1.9	1.0	Natih A
15-2012	23.0	2.0	2.1	Natih A
16-2012	23.2	2.2	3.8	Natih A
17-2012	23.6	2.2	5.2	Natih A
57-2012	23.5	2.2	5.2	Natih A
18-2012	25.3	2.0	6.5	Natih A
19-2012	23.9	2.4	7.6	Natih A
20-2012	23.8	2.6	8.5	Natih A
21-2012	23.5	2.5	9.7	Natih A
22-2012	23.3	3.5	11.6	Natih A
58-2012	24.3	3.4	11.6	Natih A
62-2012	23.8	3.6	12.9	Natih A
63-2012	24.2	3.2	20.5	Natih A
64-2012	24.6	3.0	29.1	Natih A
65-2012	24.7	2.4	35.5	Natih B
61-2012	24.9	2.3	38.4	Natih B
59-2012	25.1	2.3	49.1	Natih B
60-2012	25.2	1.8	49.1	Natih B

Note: Depth below top surface of Al Raheba outcrop.

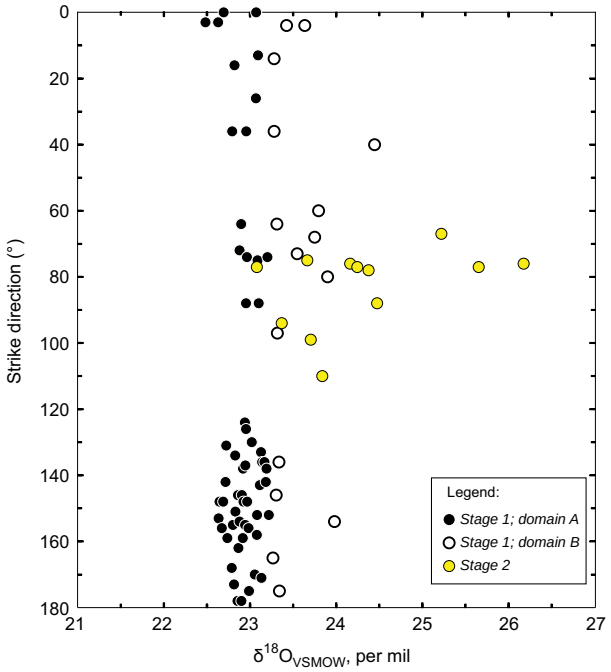

Fig. 11. Cross-plot showing variations in $\delta^{18}O$ composition of veins as a function of vein strike. The $\delta^{18}O$ composition of veins within domain B of Stage 1 is slightly higher than Stage 1 domain A veins within the entire range of vein strike directions. The most ^{18}O-enriched veins occur only within the approximately EW-striking, late fault vein.

the vein margin and the vein interior (Fig. 12A). Additionally, where Stage 1 veins crosscut another, differently oriented Stage 1 vein, the two veins can have a significantly different C-isotope composition (Fig. 12B). Furthermore, the development of the younger vein does not appear to have perturbed the C-isotope composition of the adjacent parts of the older vein (Fig. 12B). Although the Stage 2 calcite has only a small variation in $\delta^{13}C$ composition, up to 2 ‰ variation in $\delta^{18}O$ may occur across the vein (Fig. 12C). This variation is comparable to the maximum variation along the 10 m strike length of the entire Stage 2 fault.

DISCUSSION

Constraints on timing of vein formation

In the foreland basin approximately 100 km SW of our study area, Mesozoic limestones of the same sequence are porous hydrocarbon reservoirs (10–30% primary porosity; cf. Wagner 1990). In contrast, in our study area, the limestones have near-zero porosity (Wagner 1990). This compaction is inferred to be associated with the overburden of the overriding Hawasina and Samail thrust sheets. Although the presence of mechanical twinning points to plastic deformation after the veins were formed (Groshong 1988), the steeply dipping Stage 1 veins do not show evidence for significant vertical shortening during compaction (such as folding, compaction halos, or crosscutting by bedding-parallel stylolites, cf. Nollet *et al.* 2005). Therefore, we infer that most of the compaction and associated porosity loss occurred prior to Stage 1 veining. Thus, the development of the Al Raheba vein mesh is interpreted to have occurred in the late stages of, or after the emplacement of Hawasina and Samail nappes between 90 and 70 Ma (cf. Searle 2007). Some of the pore-filling cements (e.g., Fig. 5A) could have formed during the first burial phase or even during emergence of the platform before

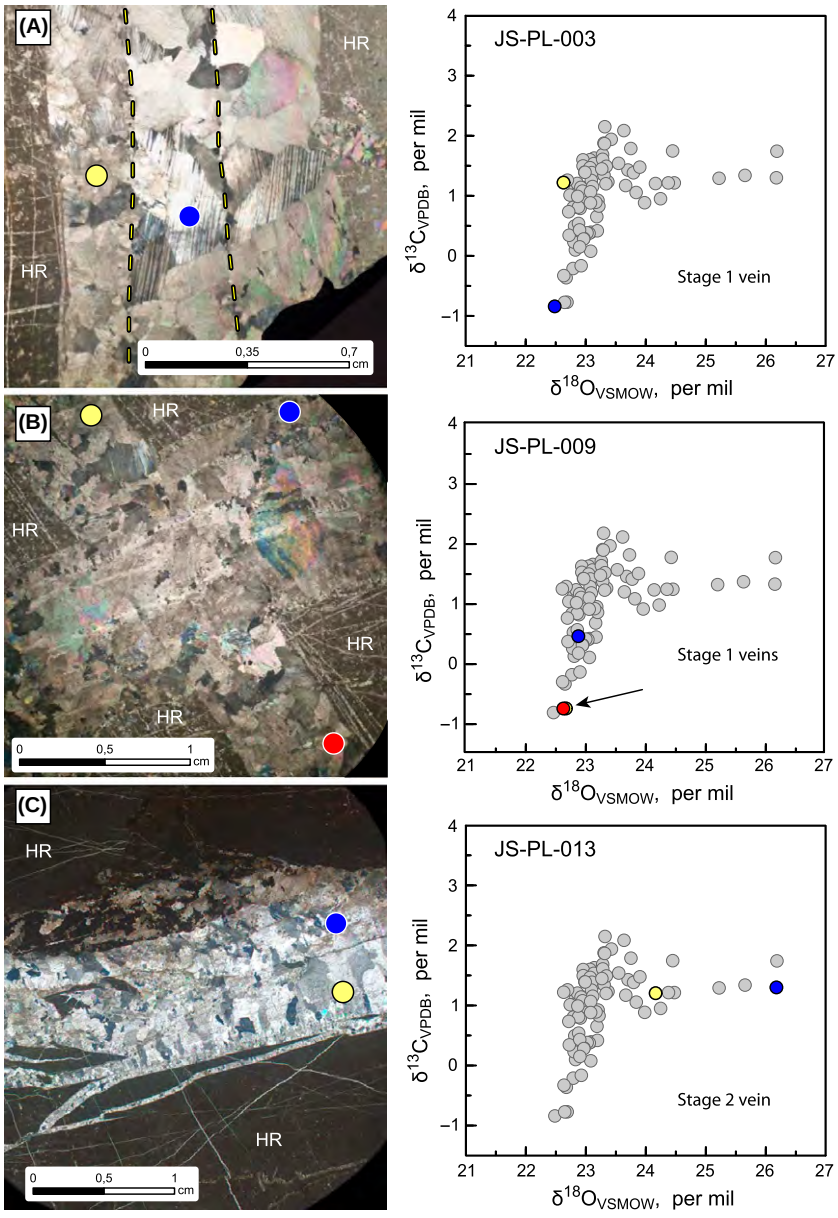

Fig. 12. Three examples of variations in C/O isotopic compositions within veins. Vein microstructure and locations of analyses (colored circles) are shown on the left; isotopic compositions of veins are illustrated on the right. For reference, the isotopic compositions of all measured vein calcites are indicated by gray circles. All thin sections are oriented parallel to bedding. North is up in all micrographs. (A). The micrograph shows a 1-cm-wide calcite extension vein (Stage 1) with three visible subdomains (indicated). The leftmost domain and the middle domain have almost the same $\delta^{18}O$ composition, but the difference in $\delta^{13}C$ is about 2 ‰. (B). Comparison of isotopic compositions near intersection of two Stage 1 veins. Note the C/O isotopic composition of the NW-striking vein (red and yellow circles) is constant on either side of the vein intersection, whereas the $\delta^{13}C$ composition of the NE-striking vein (blue circle) is 1.3 ‰ higher than the earlier vein. The black arrow in the right-hand side chart shows position of yellow data point. (C). Two different sites within a microstructurally complex, Stage 2 fault vein have a similar $\delta^{13}C$ composition, but a significantly different $\delta^{18}O$ composition.

the nappe emplacement. These are always crosscut by veins.

Several generations of veins at high angles to bedding have been postulated after nappe emplacement (Hilgers *et al.* 2006; Holland *et al.* 2009b; Holland & Urai 2010; Virgo & Arndt 2010). E-W-trending normal faulting and associated vein formation were interpreted to have taken place after these events. This normal fault system is regionally developed and exposed in an area covering at least 200 km^2. We interpret the Stage 2 fault as part of the set of E-W-trending normal faults (locally reactivated in strike-slip) described by (Holland *et al.* 2009b; Virgo *et al.* 2013b; Gomez-Rivas *et al.* 2014) elsewhere in the Jebel Akhdar anticline. This fault population may be related also to Campanian (approx 84–72 Ma) normal faulting in the foreland, outboard of the thrust sheets (Filbrandt *et al.*

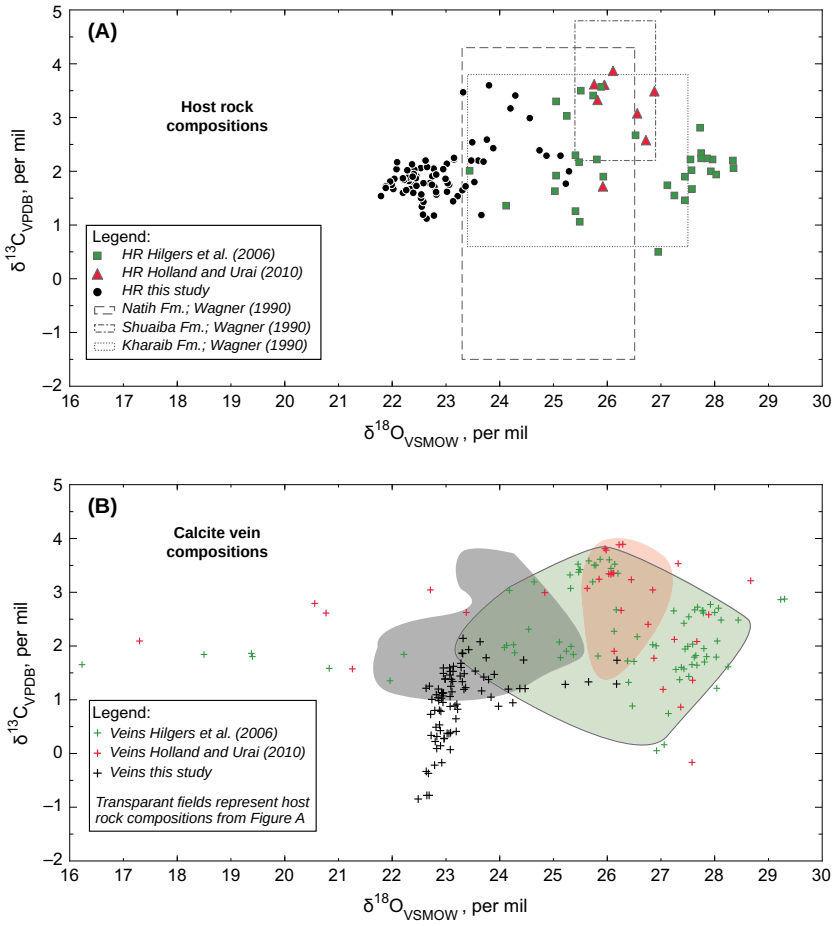

Fig. 13. The C/O stable isotope compositions (host rocks in figure A; vein calcites in figure B) of this study (in black) with respect to the isotopic compositions of calcite veins and limestones from earlier studies elsewhere in the Jebel Akhdar. Hilgers *et al.* (2006) analyzed various generations of calcite veins hosted by Cretaceous limestone across the entire Jebel Akhdar (data in green). The ranges for the Natih, Shuaiba, and Kharaib Formation limestones published by Wagner (1990) are shown in figure A. Data published by Holland & Urai (2010) is shown in red. Both studies' data indicate a large variation in vein $\delta^{18}O$ (approximately 15 ‰), whereas the variation in $\delta^{13}C$ is comparable to that found in this study (approximately 4 ‰). Most of the VHB limestones are significantly more ^{18}O depleted than those of previous studies. Most veins analyzed in this study plot in a field that is not occupied by data of Hilgers *et al.* (2006) and Holland & Urai (2010).

2006). The 15° dip of bedding in the study area is interpreted as postdating formation of the E-W faults (Virgo *et al.* 2013b), forming during Late Miocene to Pliocene development of the Jebel Akhdar anticline (Glennie 1995; Poupeau *et al.* 1998; Searle 2007).

Fracture-controlled fluid pathways

The Stage 1 vein mesh forms a highly interconnected and closely spaced network of veins at high angle to bedding. Segments of the mesh have various strike orientations, but are dominated by veins with a 160–180° strike. The lateral extent of the vein mesh is nearly two orders of magnitude larger than its vertical extent. Stage 1 vein development is thus strongly stratabound, confined to three beds with a total thickness of 3.5 m. There is no Stage 1 vein development immediately below these beds. Although direct outcrop observation is not possible at this location, we suspect that the Al Raheba Stage 1 vein mesh is not directly connected to veins in the overlying Muti Formation.

The morphology and interconnectivity of the Stage 1 vein mesh are interpreted to have facilitated fracture-controlled fluid flow parallel to bedding. The dominance of veins with 160–180° strikes is expected to have led to strong anisotropy of fracture permeability. The common crack-seal microstructures in Stage 1 veins suggest that there was only a limited number of open fractures at any time during this stage.

As the Stage 2 fault is approximately 10 m long and has a maximum dip separation of 10 cm, we interpret that it penetrates at least 10 m below the VHB (Walsh *et al.* 2003; Kim & Sanderson 2005), and the dilatant fracture in which this vein formed could access fluids from below the VHB. Larger faults of this generation commonly offset the contact with the units overlying the Natih, and we infer that the Stage 2 fault penetrates the overlying Muti Formation.

Isotopic variations in the host rock

The lowest $\delta^{18}O$ values (21.8 ‰) in the VHB are 1.4 ‰ lower than the lowest $\delta^{18}O$ values found by Wagner (1990) in a regional study of Cretaceous limestones in northern Oman. His results indicate the most ^{18}O-depleted compositions (approximately 23.3 ‰) occur near the top of the Natih A member. These composi-

tions are up to 4 ‰ lower than typical marine limestones of comparable age. At deeper levels in the stratigraphy, some 250 m below the Natih A member, the top of the Natih E member is also ^{18}O depleted (minimum values of approximately 23.9 ‰). The unusually low $\delta^{18}O$ compositions are recognized regionally and are interpreted to result from diagenetic alteration by infiltration of meteoric water during periods of subaerial exposure of the Natih Formation (Scott 1990; Wagner 1990; van Buchem *et al.* 2002; Grélaud *et al.* 2006, 2010; Searle 2007). This suggests exceptionally intense, early diagenetic alteration at the top of the Natih A member at Al Raheba.

The C/O composition of the proximal host rocks is more tightly clustered than the composition of the distal host rock (VHB) and defines a compositional field within domain A of Stage 1 vein compositions (Fig. 9). It is inferred that proximal host rock has been altered by fluid–rock interaction immediately adjacent to Stage 1 veins during their formation. The proximal host rocks tend to be slightly ^{13}C depleted compared with the distal host rock (VHB) (Fig. 9). About 50% of the measured limestone compositions fall outside the ranges found by previous studies in the Jebel Shams area (Hilgers *et al.* 2006; Holland & Urai 2010). This is because these studies analyzed samples from deeper in the stratigraphy, where syn-diagenetic ^{18}O depletion of marine limestones did not occur (Fig. 13).

Interpretation of isotopic variations within veins

Stage 1 extension veins

As the Stage 1 vein mesh is strongly stratabound within a 3.5-m stratigraphic interval, fluid migration is likely to have been dominated by flow paths parallel to bedding, rather than across bedding. There are no obvious Stage 1 fracture-controlled pathways linking the VHB to lower or higher parts of the stratigraphic succession in the study area.

The $\delta^{13}C$ composition of the most ^{13}C-depleted veins in Stage 1 domain A (−0.8 ‰) is not in equilibrium with the host rock (VHB), which has a minimum $\delta^{13}C$ of 1.5 ‰ in the Al Raheba area (Fig. 9). Approximately 65% of Stage 1 veins have significantly lower $\delta^{13}C$ than their host rock (VHB), with $\delta^{13}C$ extending down to −0.8 ‰ (Fig. 9B). In the stratigraphy within the 50 m below the VHBs, there are no limestones with $\delta^{13}C$ <1.8 ‰ (Fig. 10). Accordingly, it is unlikely that the ^{13}C depletion trend in Stage 1 domain A veins is related to influx of fluids buffered by nearby low $\delta^{13}C$ limestones. However, there are several other mechanisms for producing ^{13}C-depleted fluids:

(1) Isotopic exchange between CO_2-bearing fluids and carbon in organic matter (usually with very low $\delta^{13}C$) (Valley & O'Neil 1981; Kerrich 1990).
(2) Oxidation of light hydrocarbon fluids (e.g., CH_4) to CO_2 by passage of reduced fluids through oxidizing rock types (e.g., Fe^{3+}-bearing rock types).
(3) Progressive isotopic fractionation of very low total carbon content $\sum C$ fluids along the fluid pathway (e.g., Abart & Pozzorini 2000).
(4) Generation of low $\delta^{13}C$ CO_2 fluids by oxidation, decarboxylation, or hydrolysis of reduced carbon during progressive heating, for example in stylolites (Ohmoto & Rye 1979; Kerrich 1990).

Interaction of CO_2-bearing fluids with reduced carbon (e.g., kerogen) may induce ^{13}C depletion in vein carbonates (Kerrich 1990). At temperatures <300°C, isotopic exchange between reduced carbon, fluids, and calcite is kinetically inhibited (Valley & O'Neil 1981), but partial exchange is possible (Kerrich 1990). Maximum paleotemperatures in the Natih Formation near Al Raheba, inferred from bitumen reflectance (Fink 2013) are between 240 and 320°C. The content of primary, detrital organic matter is typically very low in carbonate mudstones (<0.3%), but may be locally enriched by pressure solution (di Primio & Leythaeuser 1995).

Equilibrium fractionation between reduced carbon and calcite at 300°C is approximately +11 ‰ (Bottinga & Craig 1968). As organic carbon $\delta^{13}C$ composition is typically -26 ± 7 ‰, $\delta^{13}C$ of calcite precipitated from fluid buffered by reduced carbon could be as low as -15 ± 7 ‰. Accordingly, even though isotopic exchange may be inhibited at the temperatures of vein formation, very little isotopic exchange between CO_2 and organic carbon is required to achieve the observed ^{13}C depletion of 2 ‰ relative to calcite in the host rock.

Progressive fractionation of C isotopes can occur downstream along flow paths in H_2O-rich fluids in which ΣC is very low. The ^{13}C is preferentially fractionated to the solid phase (calcite) as it precipitates, thereby leaving the fluid phase ^{13}C depleted. A fluid having an initial isotopic composition in equilibrium with the host rock, but low $\sum C$, could then progressively change to a more ^{13}C-depleted composition. This change can be indicated by vein calcite becoming more ^{13}C-depleted. For flow driven by persistent gradients in hydraulic head, C-isotope fractionation should lead to a persistent gradient in C-isotope composition of veins downstream along a flow path. The lack of systematic spatial variations in C-isotope composition of veins across the Al Raheba vein mesh (especially along the inferred NNW high-permeability direction) indicates that fractionation might not have been a significant factor influencing the ^{13}C depletion trend in Stage 1 (domain A) veins.

The B member of the Natih Formation is a hydrocarbon source rock, as are some limestones deeper in the Mesozoic sequence (Terken 1999; Terken *et al.* 2001). Oxidation of light hydrocarbons (e.g., CH_4) can produce low $\delta^{13}C$ CO_2. However, as a source of oxidants (such as red-

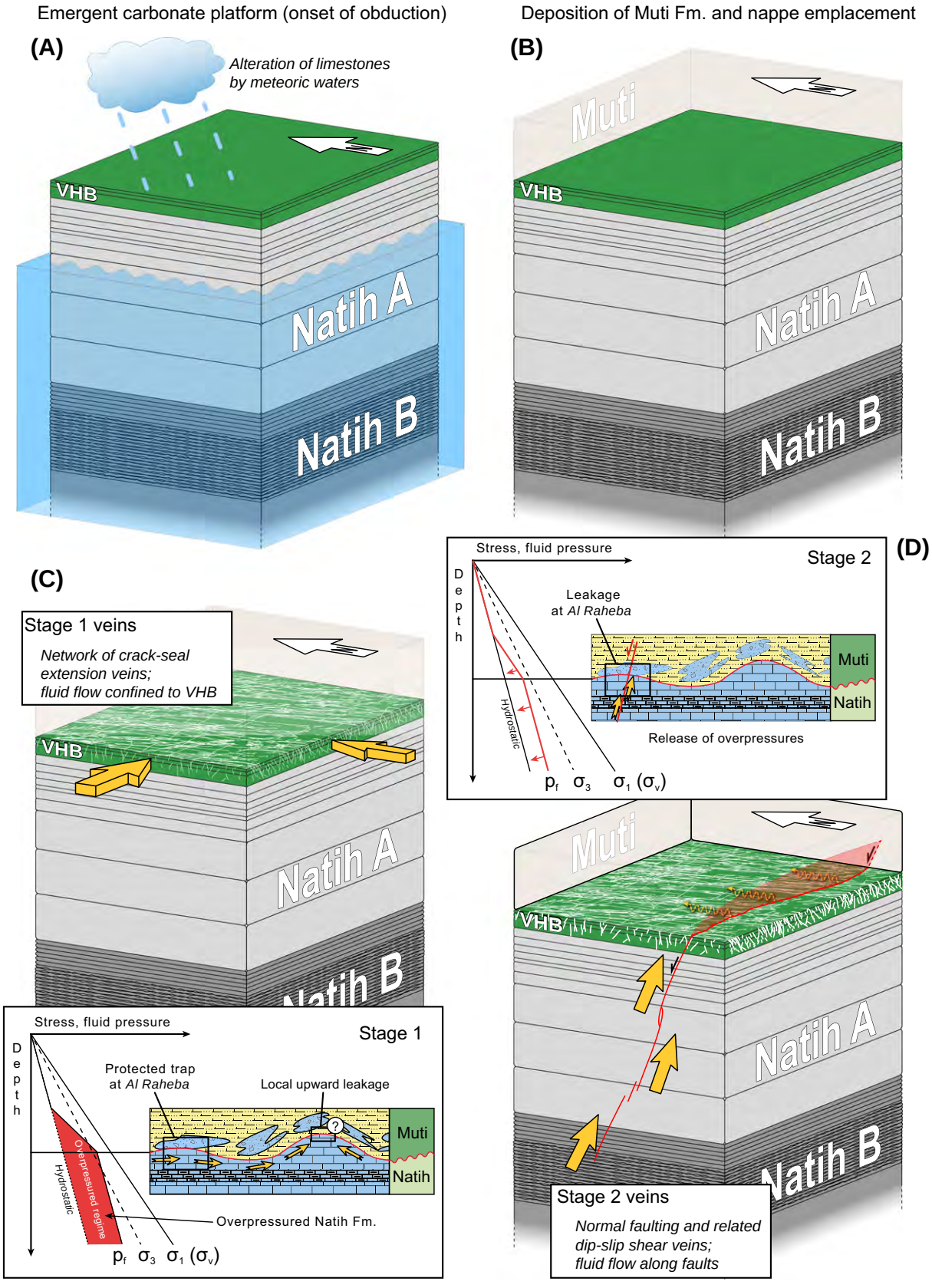
Emergent carbonate platform (onset of obduction)
(A)
Alteration of limestones by meteoric waters
VHB
Natih A
Natih B
Deposition of Muti Fm. and nappe emplacement
(B)
Muti
VHB
Natih A
Natih B
(C)
Stage 1 veins
Network of crack-seal extension veins; fluid flow confined to VHB
VHB
Natih A
Natih B
Stress, fluid pressure
Stage 1
Depth
Protected trap at Al Raheba
Local upward leakage
Muti
Natih
Overpressured regime
Hydrostatic
Overpressured Natih Fm.
pf σ3 σ1 (σv)
(D)
Stress, fluid pressure
Stage 2
Depth
Leakage at Al Raheba
Muti
Natih
Hydrostatic
Release of overpressures
pf σ3 σ1 (σv)
Muti
VHB
Natih A
Natih B
Stage 2 veins
Normal faulting and related dip-slip shear veins; fluid flow along faults

bed sequences) is not apparent in the local stratigraphy, it is unlikely that mixing of oxidized hydrocarbons with fluids in the vein mesh has influenced the C-isotope composition of fluids and calcite veins.

In the prograde thermal regime expected in the limestone sequence in response to rapid burial during nappe emplacement, low $\delta^{13}C$ CO_2 can be produced by thermal decarboxylation of organic matter (Kerrich 1990). Similarly, reaction between water and reduced organic matter can lead to hydrolysis and oxidation of the organic matter and consequent production of low $\delta^{13}C$ CO_2 (Kerrich 1990). CO_2 produced by thermal decarboxylation, hydrolysis, or oxidation of organic matter reflects the $\delta^{13}C$ composition of the organic matter, and typically has a $\delta^{13}C$ (CO_2) less than about −20 ‰ (Irwin *et al.* 1977 Curtis, 1978; Smith & Gould, 1980; Reuning *et al.* 2009). As the ^{13}C composition of the most ^{13}C-depleted Stage 1A veins is <2 ‰ lower than the VHB, only a very small proportion of organically derived CO_2 (generated by decarboxylation, hydrolysis, or oxidation) is needed to produce the observed C-isotope compositional range.

di Primio & Leythaeuser (1995) have shown how effectively pressure solution can locally enrich organic matter in carbonate rocks. In the VHB, organic matter has been enriched at pressure solution seams (stylolites). The local enrichment of organic matter at pressure solution seams is a prerequisite for effective petroleum generation and expulsion as well as CO_2 production at subsequent stages of deeper burial and organic matter catagenesis (Leythaeuser *et al.* 1995). The μFT-IR results presented in Fig. 8 provide support for this model. During Stage 1, any fracture crosscutting a stylolite would likely access CO_2 that was produced from the organic matter. Given that (i) common local enrichment of organic matter occurs at pressure solution seams at high angle to the veins, and (ii) large fluid–rock reaction surfaces were generated by repeated and dense fracturing, we infer that low $\delta^{13}C$ CO_2 was derived from organic matter during Stage 1. This then mixed with fracture-filling fluids to precipitate vein calcite that was up to 2 ‰ ^{13}C-depleted relative to the VHB. This is in agreement with the strong spatial variability in the $\delta^{13}C$ composition of Stage 1 vein calcite (Fig. 12).

Stage 1 domain B veins are slightly depleted in ^{13}C relative to the VHB, but are up to 1 ‰ more ^{18}O-enriched. The composition of the Stage 1B veins is consistent with buffering of $\delta^{13}C$ composition predominantly by the VHB, but with much less influence of ^{13}C-depleted fluids than is the case for Stage 1A veins. However, consistent ^{18}O enrichment relative to the VHB probably indicates an influence of fluids that were up to 1 ‰ more ^{18}O-enriched than the VHB. This enrichment is plausibly related to influx of fluids that were buffered by reaction with the narrow band of ^{18}O-enriched limestones in the Natih A member approximately 8 m below the VHB.

Alternatively, externally buffered fluids could have had a $\delta^{18}O$ composition influenced by reaction with deeper Natih B limestones, or higher $\delta^{18}O$ limestones even deeper in the Mesozoic sequence. However, the apparent lack of macroscopic veins that connect at depth with the Natih B member during Stage 1 likely precludes transport of fluids over significant vertical distances during Stage 1. The influx of deeper, more ^{18}O-enriched fluids into the VHB was apparently very limited until the growth of the normal fault during Stage 2.

Stage 2 fault veins

The Stage 2 calcite has a narrow range in $\delta^{13}C$ but is ^{18}O-enriched by up to 3 ‰ relative to the average host rock (VHB) composition; the maximum ^{18}O composition is 26.2 ‰ (Fig. 9B). The linear trend of ^{18}O enrichment of Stage 2 calcite relative to the composition of the VHB is consistent with precipitation of vein calcite from externally

Fig. 14. Diagrammatic illustration of fluid flow regimes and fluid pathways prior to, and during vein mesh development at the Al Raheba pavement. (A). The emergence of the carbonate platform may reflect the onset of thrusting from the north. During this stage, meteoric waters altered the original limestone composition, causing ^{18}O depletion. (B). Deposition of the Muti Formation in a foreland basin that formed in front of the obducted Hawasina and Samail thrust sheets (nappes). (C). After the nappe emplacement, a mesh of crack-seal extension veins developed (Stage 1 veins; indicated by white lines). As the mesh is localized within the three uppermost layers of the Natih A member (VHB, in green), fluid flow is interpreted to have been largely parallel to bedding within the VHB (yellow arrows). Fluid flow is inferred to have been directed toward a local leakage point in the vicinity of Al Raheba at overpressured conditions (red polygon), with fluid pressure episodically exceeding σ_3, the minimum principal stress (see stress–depth plot). Strong anisotropy of vein orientations may have constrained most flow along a NNW-SSE direction. Isotopic exchange between migrating fluids and both the overlying Muti Formation (seal) and underlying limestone layers might have occurred during Stage 1. Note the heterogeneous distribution of calcareous siltstones (yellow) and limestone breccias (blue) in the Muti Formation (inset sketch is not to scale). Principal stresses (σ_1, σ_3), the vertical load (σ_v), and fluid pressures (p_f) are plotted against depth and illustrate the stress state at Al Raheba during Stage 1. The regime of fluid overpressures is illustrated by a red polygon. (D). During Stage 2, the late E-W-striking fault penetrated beneath the VHB and potentially connected hydraulically with the Natih B member. Stage 2 vein compositions indicate oxygen isotope buffering by limestones more ^{18}O-enriched than the VHB, possibly in a zone 5–10 m below the VHB, or by Natih B limestones at least 40–50 m below the VHB (see also Fig. 10). Fluid exchange with the overlying Muti Formation might also have occurred during Stage 2. Note the inferred fault plane drawn as transparent, red polygon. During Stage 2, high fluid pressures at Al Raheba are released through the fault cutting into the overlying seal (Muti Formation). Principal stresses (σ_1, σ_3), the vertical load (σ_v), and fluid pressures (p_f) are plotted against depth and illustrate the stress state at Al Raheba during Stage 2. The differential stress (σ_1–σ_3) is larger than during Stage 1. For repeated failure, p_f in the VHB was still overpressured, but could fall back toward hydrostatic fluid pressures (indicated by red arrows) after each rupture event.

sourced, ^{18}O-enriched fluids, which were progressively ^{18}O buffered by the VHB.

Variations in $\delta^{18}O$ compositions of limestones beneath the VHB provide some constraints on potential sources of fluids having $\delta^{18}O$ as high as 26.2 ‰. Such values are broadly consistent with buffering of fluid composition by Cretaceous limestones with $\delta^{18}O$ composition unaffected by diagenetic alteration overprints (Wagner 1990; Veizer *et al.* 1999).

At a depth of 5 m below the VHB, there is a narrow interval in which $\delta^{18}O$ reaches a maximum of 25.3 ‰. The most ^{18}O-enriched Stage 2 calcites have $\delta^{18}O$ about 1 ‰ higher (Figs 9 and 10). The one sample analyzed from this interval has a $\delta^{18}O$ value of 25.3 ‰. But this is about 1 ‰ lower than the most ^{18}O-enriched Stage 2 calcite (Figs 9 and 10). Rock buffering of the O isotope composition of water passing through this layer could lead to precipitation of vein calcite in the VHB with $\delta^{18}O$ as high as 25.3 ‰, but not as high as 26.2 ‰.

At still deeper levels, in sequence III-4 of the Natih B member, limestones do have an oxygen isotope composition that is comparable to those of the most ^{18}O-enriched Stage 2 calcites (Figs 9 and 10). The most ^{18}O-enriched limestones in our small sample suite from sequence III-4 are approximately 1 ‰ more ^{18}O-depleted than the most ^{18}O-enriched Stage 2 calcite in the VHB. However, limestones in the more extensive sample suite of Wohlwend & Weissert (2012), which were collected up to 9 km SE of our field area, do have an ^{18}O composition very similar to the most ^{18}O-enriched Stage 2 fault veins (Fig 9).

On the assumption that the ^{18}O composition of fluids in the limestone sequence is controlled primarily by buffering by limestone and its components along fracture-controlled fluid pathways, it is proposed that the O isotope composition of fluids percolating through the Stage 2 fault were buffered originally by limestones with normal Mesozoic $\delta^{18}O$ compositions. Although a thin band of such limestone occurs a few meters beneath the VHB, limestones with $\delta^{18}O$ >24 ‰ dominate the stratigraphic sequence in the Natih B member deeper than 50 m below the VHB (Figs 10 and 14). Involvement of Natih B limestones in buffering fluid ^{18}O composition requires that the small Stage 2 fault was hydraulically connected to this stratigraphic level. Given the small strike extent of the fault (10 m), it is unlikely the fault penetrates as deep as 50 m. Accordingly, the fluid pathway must have involved several hydraulically linked fractures (Fig. 14).

An alternative possibility is that ^{18}O-enriched compositions of Stage 2 calcites, relative to the VHB limestone, may be related to fluids that were buffered by limestones at even deeper stratigraphic levels and then migrated through fault-fracture networks into the VHB. For example, limestones at deeper levels in the Mesozoic sequence typically have $\delta^{18}O$ in the range 25–28.5 ‰ (Wagner 1990; Hilgers *et al.* 2006). However, this model requires that the length scales on which fluids become ^{18}O buffered during fracture-controlled flow in limestones were in excess of hundreds of meters. Although the length scales of such buffering are dependent on parameters such as time-integrated fluid flux and flow rate (e.g., Abart & Pozzorini 2000; Cox 2007), the finding that a large proportion of Stage 2 calcite samples have a $\delta^{18}O$ composition that is close to rock-buffered by the VHB indicates that rock buffering has occurred on length scales much shorter than hundreds of meters.

A further possibility is that the ^{18}O-enriched Stage 2 fault vein samples reflect the influence of ^{18}O fractionation during down-temperature (i.e., upwards) migration of the fluids in the fracture-controlled flow regime. Fluids with a composition buffered at 300°C by limestones having $\delta^{18}O$ of 28 ‰ could precipitate calcite with $\delta^{18}O$ of 31 ‰ at 250°C, or 34.7 ‰ at 200°C (Kim & O'Neil 1997). The lack of such extreme ^{18}O enrichment in Stage 2 fault veins, together with the apparent length scales on which O isotope buffering apparently occurs along fluid pathways (as discussed above), indicates that effects of isotopic fractionation related to down-temperature flow of fluids are minimal. Certainly, any temperature gradient effects on ^{18}O fractionation between the Natih B limestones, and the VHB some 50 m stratigraphically higher, are negligible compared with effects related to rock buffering by limestones with a $\delta^{18}O$ composition several per mil higher than the VHB.

Potential isotopic exchange with the Muti Formation

The potential influence of limestones and calcareous siltstones in the overlying Muti Formation on the C/O isotopic character of Stage 1 veins in the uppermost Natih member cannot be constrained using the available data. There is a lack of calcareous sedimentary rocks and a scarcity of veins in outcrops of the Muti Formation within a few tens of meters of the Muti-Natih contact at Al Raheba. This suggests that the Muti Formation is not involved in buffering the composition of fluids associated with vein development in the Natih A member.

The possibility remains that the isotopic composition of Stage 2 fluids may have been influenced by fluid–rock reaction with marine carbonates which occur locally within the Muti Formation overlying the VHB. However, lack of outcrop of limestones or calcareous mudstones in the Muti Formation in the vicinity of our study area precludes further study of this aspect.

Evolution of structures and fluid flow regimes

The Stage 1 vein mesh is interpreted to have grown progressively by increases in vein length and width, along with episodic nucleation of new fractures and veins. With ongoing evolution of the mesh, new fractures have inter-

acted more and more with existing veins that act as mechanical anisotropies and heterogeneities (Virgo *et al.* 2013a).

Processes controlling the C/O isotope composition of calcite veins during Stage 1 are confined predominantly to the VHB. Vein growth during Stage 1 was dominated by largely stratabound, fracture-controlled flow within the VHB. During Stage 2, processes controlling the isotopic composition of calcite are confined to a dilatant normal fault penetrating the stratigraphy beneath, and possibly above the VHB. Stage 2 vein growth was governed largely by localized, fault-controlled fluid flow at a high angle to bedding. The change from the Stage 1 to Stage 2 flow regime is thus marked by a transition from predominantly bedding-parallel, fracture-controlled flow within an areally extensive fracture network within the VHB, to the development of a more deeply penetrating, more localized, fault-controlled flow regime which allowed influx to the VHB of externally buffered fluids in Stage 2.

The composition of Stage 1A veins reflects rock buffering by ^{18}O of the VHB, along with small but variable addition of ^{13}C-depleted CO_2, interpreted as being derived from local fluid reaction with organic matter in the VHB. The slightly different composition of Stage 1B veins is interpreted to reflect either (i) shutdown of the source of ^{13}C-depleted fluids, or (ii) rock buffering of $\delta^{13}C$ by the VHB, along with continued ingress of slightly ^{18}O-enriched fluids which were buffered partly by the sub-VHB limestones. This could reflect some limited, late downward growth of the fracture network into sub-VHB limestones.

The transition from Stage 1 extensional vein formation to Stage 2 fault vein formation is associated with a distinct change in C/O isotopic character of veins and the fluids that generated them. Although most Stage 2 fault veins are slightly ^{13}C-depleted relative to the VHB, indicating influx of only a very minor component of ^{13}C-depleted fluid, the key difference between Stage 1 and Stage 2 fault veins is that the latter are mostly ^{18}O-enriched relative to Stage 1 veins. Importantly, isotopic composition and structural relationships indicate that the Stage 1 vein mesh was sealed and de-activated as a fluid pathway by the commencement of Stage 2.

The rock volume influenced by fracture-controlled flow within the VHB during Stage 1 is orders of magnitudes higher than in Stage 2. This suggests that exposure of migrating fluids to large fracture surface areas during Stage 1 has facilitated more effective local rock buffering of ^{18}O composition than was the case during Stage 2.

Importantly, the Stage 1 and Stage 2 veins did not provide fracture pathways that were continuously open to flow. Crack-seal microstructures indicate that at any instant, fracture apertures were mostly less than several tens of microns. Host rock inclusion bands are interpreted to indicate that the majority of fractures grew at the interface between veins and host rock. The growth of typical veins required hundreds to a few thousand increments of fracture opening and sealing. Fluid pathways therefore repeatedly switched between high-permeability and low-permeability states. Accordingly, at any one site, flow must have been episodic. It is, as yet, unclear how pathways have switched around the mesh during Stage 1, but the complex crosscutting relationships between veins of various orientations suggest that pathways were geometrically tortuous (cf. Barnhoorn *et al.* 2010). It is also not clear whether the Stage 1 vein mesh grew by episodic pulses of synchronous permeability enhancement and flow across the entire mesh, or whether at the mesh scale, flow was quasi-continuous, with permeability switching (crack-seal) occurring asynchronously at scales of individual vein segments.

Stress, strain, and fluid pressure regimes

The orientation of the Stage 1 extension veins implies that σ_3 was parallel to bedding during their formation (Virgo *et al.* 2013b). The total extensional strain in the bedding plane associated with Stage 1 vein formation involved stretching in various directions within the bedding plane. The maximum stretch is in ENE direction, perpendicular to the dominant vein trend. This stretching direction is slightly inclined to the small, NE-trending ductile stretch indicated by grain-scale strain fringes (Fig. 7). The strain associated with vein opening, although small, is transitional between pure flattening strain and plane strain. This is consistent with vertical shortening in response to a near-vertical maximum principal stress during Stage 1, with the dominant orientation for σ_3 ENE trending. The presence of extension veins in variable orientations requires that σ_3 and σ_2 rotated in the bedding plane during Stage 1. A vertical σ_1 during Stage 1 is consistent with vein formation after emplacement of the Hawasina and Samail nappes.

As the NNW-trending Stage 1 veins are commonly overprinted by steeply dipping, NW-trending stylolites, and the latter are, in turn, commonly cut by NW and WNW-trending Stage 1 veins, it is inferred that σ_1 was nearly parallel to bedding and trending NE-SW, at least transiently during the growth of the Stage 1 vein mesh. A lack of extension veins with orientations consistent with the stress field during formation of the tectonic stylolites does not allow a determination of whether the stress regime was normal faulting, contractional, or strike-slip. Nevertheless, it is clear that major changes of the stress field occurred during the development of the Stage 1 vein mesh.

Assuming a bulk density of 2800 kg m^{-3} (cf. Al-Lazki *et al.* 2002) and an overburden of 7 km (Searle 2007), the vertical stress (σ_V) is estimated to have been approximately 190 MPa during vein development. For conditions of extensional failure, the differential stress (σ_1–σ_3) needs to be <4T (where T is the tensile strength) (Secor 1965).

Assuming a tensile strength of <10 MPa, the minimum value of the least principal stress (σ_3) is estimated as at least 150 MPa.

Under compressional stress states at depth in the crust, extension failure requires that pore fluid pressure, $P_f = \sigma_3 + T$, that is, a minimum of approximately 160 MPa. The pore fluid factor λ_v (P_f/σ_v) required to initiate failure is thus at least 0.84 and probably higher. Our interpretation is consistent with that of Hilgers *et al.* (2006), who also argued for near-lithostatic fluid pressures during vein formation episodes elsewhere in the Jebel Akhdar anticline. Such hydraulic extension fracturing could have been driven by fluid injection and/or by decrease of σ_3 (cf. Cox 2010).

The widespread presence of antitaxial crack-seal microstructures in Stage 1 veins indicates that repeated fracturing of existing veins was more favored than nucleation of new fractures in intact limestone (Holland & Urai 2010). Accordingly, the tensile strength of the bulk rock mass is interpreted to have decreased with evolution of the vein mesh.

Repeated shear failure during the growth of the Stage 2 fault requires higher (σ_1–σ_3) than during Stage 1 (e.g., Cox 2010). High pore fluid factors are still required as indicated by the dilatancy of the fault, but less than for Stage 1.

Fluid overpressures and lateral fluid flow

Following Swarbrick *et al.* (2002) fluid overpressures can be a consequence of undercompaction or inflation. In agreement with Hilgers *et al.* (2006), we interpret the high pore pressures at Al Raheba as a consequence of rapid burial during nappe emplacement. While it is not clear how much porosity loss in the VHB occurred by diagenetic cementation before nappe emplacement, the overlying fine-grained sedimentary rocks of the Muti Formation are interpreted to have provided an effective seal and inhibited upward-directed fluid flow at Al Raheba, as was the case for the petroleum systems in the foreland (Terken 1999).

Under these conditions, hydraulic fracturing can create bedding-parallel and bedding-discordant fluid pathways. The Stage 1 network provides evidence for stratabound fluid transport within the VHB immediately underneath the contact with the inferred seal of the high-pressure cell (Muti Formation), because of the strong connectivity of the fractures in the crack-seal vein mesh. This lateral fluid transport could have been associated with the hydraulic gradient toward a leak point in the seal (Fig. 14C) in a structurally higher position, as described for the 'protected trap' systems in sedimentary basins (cf. Lupa *et al.* 2002; their figure 8). Alternatively, the hydraulic gradients could have been associated with the gradient in overburden stress along the nappes (Oliver 1986).

The high fluid pressures in the VHB were released episodically during Stage 2 through repeated cycles of shear failure (permeability enhancement) and intervening hydrothermal sealing on steeply dipping shear fractures, which are interpreted to have breached the seal (Fig. 14D). Significantly, in an overpressured regime, the hydraulic gradients drive upwards fluid flow. In the absence of dynamic fluid pressure drops associated with dilation during fault slip events, it is unlikely that fluids in the Muti Formation have been drawn down into the underlying VHB and influenced C/O isotopic composition of veins in the VHB.

Relation to vein meshes in thrust belts

There is a wide variety of vein networks and fluid flow regimes in thrust belts (Dietrich *et al.* 1983; Sibson 1996; Lefticariu *et al.* 2005). The Al Raheba vein mesh is not directly comparable with the more 'common' systems, because the deformation effects of the overriding Hawasina and Samail nappes are only indirectly seen in our study area. Tectonic deformation in the Natih formation is very weak, and later overprinting of the Stage 1 vein mesh is limited to dilatant Stage 2 fault veins (these are much more important where the offset of the normal faults is larger and where massive vein networks develop in the dilatant jogs; cf. Holland *et al.* 2009b). Later, broad-scale folding of the Jebel Akhdar anticline is only represented by a tilt of the exposed strata (Breton *et al.* 2004; Searle 2007; Virgo *et al.* 2013b). Therefore, the Al Raheba vein mesh is best observed as representing the early vein generations which can be much more strongly overprinted in other settings (cf. Dietrich *et al.* 1983). Another important aspect to consider is the that the overriding Hawasina and Samail nappes could well have led to an unusually rapid buildup of overpressures in the Wasia group, although many other thrust belts show close to lithostatic pressures in early vein generations (Sibson 1996; Van Noten *et al.* 2012).

CONCLUSIONS

From our observations, we propose three different fluid influx events that are recorded in the host rock and calcite veins in the Al Raheba pavement.

(1) Shortly after the deposition of the Natih A limestone, the carbonate sequence was uplifted and prone to subaerial exposure. This led to the influx of meteoric water and associated syn-diagenetic alteration of the original marine limestone stable isotope signature in the topmost part of the Natih A member. This alteration is recorded by low $\delta^{18}O$ values in the VHB. This explanation is supported by regional-scale sequence stratigraphy studies, conducted in the subsurface and in outcrop (Wagner 1990; Grélaud *et al.* 2006, 2010; Wohlwend & Weissert 2012). The O isotope composi-

tion of the topmost part of the Natih A member at Al Raheba is slightly more ^{18}O-depleted than stratigraphically equivalent limestones elsewhere in the region. Accordingly, the top of the Natih A member at Al Raheba has undergone especially intense diagenetic alteration prior to vein formation.

(2) The second event involved formation of Stage 1 extensional, crack-seal calcite veins in a predominantly fracture-controlled flow regime. Stage 1 veins mostly have a depleted ^{13}C composition relative to the VHB, but a nearly rock-buffered ^{18}O composition. They formed during largely stratabound fluid flow, under near-lithostatic fluid pressure conditions. Fluid mixing with low $\delta^{13}C$ CO_2, derived from thermal decomposition of organic matter (enriched at pressure solution seams) in the VHB, is interpreted to be responsible for producing low $\delta^{13}C$ vein calcites. The formation of a subset of Stage 1 extension veins (Stage 1B) involved fluids that were ^{18}O buffered by limestones having a composition that was slightly ^{18}O-enriched relative to the VHB. This probably indicates minor and episodic addition to the Stage 1 flow system, of fluids that had equilibrated with limestones immediately beneath the VHB.

(3) During Stage 2, the growth of an E-W normal fault created a new fluid pathway which allowed ingress to the VHB of fluids that had equilibrated with limestones that are several per mil more ^{18}O-enriched than the VHB limestones. Member B of Natih Formation, some 50 m beneath the VHB, is a potential source of such fluids, although a narrow interval of ^{18}O-enriched limestones only 5–10 m below the VHB may have contributed to buffering the O isotope composition of Stage 2 fluids.

Microstructural evidence for repeated operation of crack-seal processes, along with C/O isotopic variations within veins, indicate that Stage 1 and Stage 2 vein formation involved cyclic creation and destruction of fracture permeability, and accordingly, that vein formation occurred in an episodic flow regime.

We show that carbon and oxygen stable isotope compositions are a valuable tool to track changes in fluid flow regimes in fracture and vein meshes. The Al Raheba vein mesh evolved at large burial depth under near-lithostatic fluid pressures below allochthonous thrust sheets near a convergent plate boundary. It has evolved and grown over time and thus is not representative of a mesh of simultaneously open fractures. Compared with other, more 'common' vein systems in thrust belts, tectonic overprint of the vein mesh is weakly developed.

ACKNOWLEDGEMENTS

The authors thank Ake Fagereng and an anonymous reviewer for thorough reviews, which have improved the manuscript. Craig Manning is acknowledged for editorial guidance and choosing figure 4B as the 2014 cover image of Geofluids. We thank Lars Reuning for comments on the manuscript and especially for discussion of stable isotope results. We thank Stephan Wohlwend (ETH-Zurich) for providing stable isotope data for the Natih B and A limestones. Paul Stenhouse, Heather Scott-Gagan, Joe Cali, and Joan Cowley provided expert assistance with stable isotope analyses. We also thank Werner Kraus (fieldwork, thin sections), the German University of Technology in Oman (logistics), Jop Klaver (GIS), Radhika Patro (GIS), Daniel Rippen and Reinhard Fink (μFT-IR analysis, reflected light microscopy), and Philippe Razin (stratigraphy). The FRACS community provided valuable discussions in the field. Stephen Cox was funded by Australian Research Council Grant DP1093774. This study was carried out within the framework of DGMK (German Society for Petroleum and Coal Science and Technology) research project 718 'Mineral Vein Dynamics Modelling (FRACS),' which is funded by the companies ExxonMobil Production Deutschland GmbH, GDF SUEZ E&P Deutschland GmbH, RWE Dea AG and Wintershall Holding GmbH, within the basic research program of the WEG Wirtschaftsverband Erdöl- und Erdgasgewinnung e.V. We thank the companies for their financial support and permission to publish these results.

REFERENCES

Abart R, Pozzorini D (2000) Implications of kinetically controlled mineral-fluid exchange on the geometry of stable-isotope fronts. *European Journal of Mineralogy*, **12**, 1069–82.

Abart R, Sperb R (1997) Grain-scale stable isotope disequilibrium during fluid-rock interaction; 1, Series approximations for advective-dispersive transport and first-order kinetic mineral-fluid exchange. *American Journal of Science*, **297**, 679–706.

Abart R, Badertscher N, Burkhard M, Povoden E (2002) Oxygen, carbon and strontium isotope systematics in two profiles across the Glarus thrust: implications for fluid flow. *Contributions to Mineralogy and Petrology*, **143**, 192–208.

Agosta F, Kirschner DL (2003) Fluid conduits in carbonate-hosted seismogenic normal faults of central Italy. *Journal of Geophysical Research: Solid Earth*, **108**, 2221.

Al-Husseini MI (2010) Late Albian, Cenomanian and Turonian Natih Supersequence of Oman; type section for Orbiton 7 (103.6–89.0 Ma). *GeoArabia [Manama]*, **15**, 125–42.

Al-Lazki AI, Seber D, Sandvol E, Barazangi M (2002) A crustal transect across the Oman Mountains on the eastern margin of Arabia. *GeoArabia [Manama]*, **7**, 47–78.

Al-Wardi M, Butler RWH (2007) Constrictional extensional tectonics in the northern Oman Mountains, its role in culmination development and the exhumation of the subducted Arabian continental margin. *Geological Society, London, Special Publications*, **272**, 187–202.

Barnett DE, Bowman JR (1995) Coupled mass transport and kinetically limited isotope exchange: applications and exchange mechanisms. *Geology*, **23**, 209–12.

Barnhoorn A, Cox SF, Robinson DJ, Senden T (2010) Stress- and fluid-driven failure during fracture array growth: implications for

coupled deformation and fluid flow in the crust. *Geology*, **38**, 779–82.
Beurrier M, Béchennec F, Rabu D, Hutin G (1986) Geological map of Rustaq, Sheet NF 40–3D, Geological map of Oman (1:100 000) with Explanatory Notes. Directorate General of Minerals, Ministry of Petroleum and Minerals, Oman.
Bons PD (2000) The formation of veins and their microstructures. *Journal of the Virtual Explorer*, **02**, paper 4, doi: 10.3809/jvirtex.2000.00007.
Bons PD, Montenari M (2005) The formation of antitaxial calcite veins with well-developed fibres, Oppaminda Creek, South Australia. *Journal of Structural Geology*, **27**, 231–48.
Bons PD, Elburg MA, Gomez-Rivas E (2012) A review of the formation of tectonic veins and their microstructures. *Journal of Structural Geology*, **43**, 33–62.
Bottinga Y, Craig H (1968) Oxygen isotope fractionation between CO2 and water, and the isotopic composition of marine atmospheric CO2. *Earth and Planetary Science Letters*, **5**, 285–95.
Bowman JR, Willett SD, Cook SJ (1994) Oxygen isotopic transport and exchange during fluid flow; one-dimensional models and applications. *American Journal of Science*, **294**, 1–55.
Breton J-P, Bechennec F, Le Metour J, Moen-Maurel L, Razin P (2004) Eoalpine (Cretaceous) evolution of the Oman Tethyan continental margin; insights from a structural field study in Jebel Akhdar (Oman Mountains). *GeoArabia [Manama]*, **9**, 41–58.
van Buchem FSP, Razin P, Homewood PW, Oterdoom WH, Philip J (2002) Stratigraphic organization of carbonate ramps and organic-rich intrashelf basins: Natih formation (Middle Cretaceous) of northern Oman. *AAPG Bulletin*, **86**, 21–53.
Caputo R, Hancock PL (1998) Crack-jump mechanism of microvein formation and its implications for stress cyclicity during extension fracturing. *Journal of Geodynamics*, **27**, 45–60.
Cartwright I, Power WL, Oliver NHS, Valenta RK, McLatchie GS (1994) Fluid migration and vein formation during deformation and greenschist facies metamorphism at Ormiston Gorge, central Australia. *Journal of Metamorphic Geology*, **12**, 373–86.
Cooley MA, Price RA, Kyser TK, Dixon JM (2011) Stable-isotope geochemistry of syntectonic veins in Paleozoic carbonate rocks in the Livingstone Range anticlinorium and their significance to the thermal and fluid evolution of the southern Canadian foreland thrust and fold belt. *AAPG Bulletin*, **95**, 1851–82.
Cox SF (2007) Structural and isotopic constraints on fluid flow regimes and fluid pathways during upper crustal deformation: an example from the Taemas area of the Lachlan Orogen, SE Australia. *Journal of Geophysical Research*, **112**, B08208. doi:10.1029/2006JB004734.
Cox SF (2010) The application of failure mode diagrams for exploring the roles of fluid pressure and stress states in controlling styles of fracture-controlled permeability enhancement in faults and shear zones. *Geofluids*, **10**, 217–33.
Cox SF, Etheridge MA (1983) Crack-seal fibre growth mechanisms and their significance in the development of oriented layer silicate microstructures. *Tectonophysics*, **92**, 147–70.
Cox SF, Knackstedt MA, Braun J (2001) Principles of structural control on permeability and fluid flow in hydrothermal systems. *Reviews in Economic Geology*, **14**, 1–24.
Curtis CD (1978) Possible links between sandstone diagenesis and depth-related geochemical reactions occurring in enclosing mudstones. *Journal of the Geological Society*, **135**, 107–17.
Dietrich D, McKenzie JA, Song H (1983) Origin of calcite in syntectonic veins as determined from carbon-isotope ratios. *Geology*, **11**, 547–51.
Durney DW, Ramsay JG (1973) Incremental strains measured by syntectonic crystal growths. In: *Gravity and Tectonics* (eds De Jong KA, Scholten R), pp. 67–96, John Wiley & Sons, New York, London, Sydney, Toronto.
Eichhubl P, Boles JR (2000) Focused fluid flow along faults in the Monterey Formation, coastal California. *Geological Society of America Bulletin*, **112**, 1667–79.
Elburg MA, Bons PD, Foden J, Passchier CW (2002) The origin of fibrous veins: constraints from geochemistry. *Geological Society, London, Special Publications*, **200**, 103–18.
Esri (2012) Minimum Bounding Geometry (Data Management). In: ArcGIS Resource Center, ESRI.
Filbrandt JB, Al-Dhahab S, Al-Habsy A, Harris K, Keating J, Al-Mahruqi S, Ozkaya SI, Richard PD, Robertson T (2006) Kinematic interpretation and structural evolution of north Oman, Block 6, since the Late Cretaceous and implications for timing of hydrocarbon migration into Cretaceous reservoirs. *GeoArabia [Manama]*, **11**, 97–140.
Fink R (2013) Solid bitumen in calcite veins from the Oman Mountains: a structural, microstructural and geochemical study on hydrocarbon migration in the Natih. MSc thesis. Lehr- und Forschungsgebiet Geologie - Endogene Dynamik. RWTH-Aachen University.
Fisher JC (1951) Calculation of diffusion penetration curves for surface and grain boundary diffusion. *Journal of Applied Physics*, **22**, 74–7.
Fournier M, Lepvrier C, Razin P, Jolivet L (2006) Late Cretaceous to Paleogene post-obduction extension and subsequent Neogene compression in the Oman Mountains. *GeoArabia [Manama]*, **11**, 17–40.
Gerdes ML, Baumgartner LP, Person M, Rumble D (1995) One- and two-dimensional models of fluid flow and stable isotope exchange at an outcrop in the Adamello contact aureole, Southern Alps, Italy. *American Mineralogist*, **80**, 1004–19.
Glennie KW (1995) *The Geology of the Oman Mountains, An Outline of their Origin*. Scientific Press Ltd, Aberdeen.
Gomez-Rivas E, Bons PD, Koehn D, Urai JL, Arndt M, Virgo S, Laurich B, Zeeb C, Stark L, Blum P (2014) The Jabal Akhdar Dome in the Oman Mountains: evolution of a dynamic overpressured system. *American Journal of Science*, **314**, 1104–1139.
Grélaud C, Razin P, Homewood PW, Schwab AM (2006) Development of Incisions on a Periodically Emergent Carbonate Platform (Natih Formation, Late Cretaceous, Oman). *Journal of Sedimentary Research*, **76**, 647–69.
Grélaud C, Razin P, Homewood P (2010) Channelized systems in an inner carbonate platform setting: differentiation between incisions and tidal channels (Natih Formation, Late Cretaceous, Oman). *Geological Society, London, Special Publications*, **329**, 163–86.
Groshong RH (1988) Low-temperature deformation mechanisms and their interpretation. *Geological Society of America Bulletin*, **100**, 1329–60.
Hilgers C, Sindern S (2005) Textural and isotopic evidence on the fluid source and transport mechanism of antitaxial fibrous microstructures from the Alps and the Appalachians. *Geofluids*, **5**, 239–50.
Hilgers C, Urai JL (2005) On the arrangement of solid inclusions in fibrous veins and the role of the crack-seal mechanism. *Journal of Structural Geology*, **27**, 481–94.
Hilgers C, Dilg-Gruschinski K, Urai JL (2004) Microstructural evolution of syntaxial veins formed by advective flow. *Geology*, **32**, 261–4.

Hilgers C, Kirschner DL, Breton JP, Urai JL (2006) Fracture sealing and fluid overpressures in limestones of the Jebel Akhdar dome, Oman Mountains. *Geofluids*, **6**, 168–84.

Holland M, Urai JL (2010) Evolution of anastomosing crack–seal vein networks in limestones: insight from an exhumed high-pressure cell, Jebel Shams, Oman Mountains. *Journal of Structural Geology*, **32**, 1279–90.

Holland M, Urai JL, Muchez P, Willemse JM (2009a) Evolution of fractures in a highly dynamic thermal, hydraulic, and mechanical system; (I), Field observations in Mesozoic carbonates, Jebel Shams, Oman Mountains. *GeoArabia [Manama]*, **14**, 57–110.

Holland M, Saxena N, Urai JL (2009b) Evolution of fractures in a highly dynamic thermal, hydraulic, and mechanical system - (II) Remote sensing fracture analysis, Jebel Shams, Oman Mountains. *GeoArabia [Manama]*, **14**, 163–94.

Hudson JD (1977) Stable isotopes and limestone lithification. *Journal of the Geological Society*, **133**, 637–60.

Hughes-Clarke MW (1988) Stratigraphy and rock unit nomenclature in the oil-producing area of interior Oman. *Journal of Petroleum Geology*, **11**, 5–60.

Irwin H, Curtis C, Coleman M (1977) Isotopic evidence for source of diagenetic carbonates formed during burial of organic-rich sediments. *Nature*, **269**, 209–13.

Kamb WB (1959) Ice petrofabric observations from Blue Glacier, Washington, in relation to theory and experiment. *Journal of Geophysical Research*, **64**, 1891–909.

Kelemen PB, Hirth G (2012) Reaction-driven cracking during retrograde metamorphism: olivine hydration and carbonation. *Earth and Planetary Science Letters*, **345**, 81–9.

Kenis I, Muchez P, Sintubin M, Mansy JL, Lacquement F (2000) The use of a combined structural, stable isotope and fluid inclusion study to constrain the kinematic history at the northern Variscan front zone (Bettrechies, northern France). *Journal of Structural Geology*, **22**, 589–602.

Kerrich R (1990) Carbon-isotope systematics of Archean Au–Ag vein deposits in the superior province. *Canadian Journal of Earth Sciences*, **27**, 40–56.

Kim S-T, O'Neil JR (1997) Equilibrium and nonequilibrium oxygen isotope effects in synthetic carbonates. *Geochimica et Cosmochimica Acta*, **61**, 3461–75.

Kim Y-S, Sanderson DJ (2005) The relationship between displacement and length of faults: a review. *Earth-Science Reviews*, **68**, 317–34.

Knoop SR, Kennedy LA, Dipple GM (2002) New evidence for syntectonic fluid migration across the hinterland-foreland transition of the Canadian Cordillera. *Journal of Geophysical Research: Solid Earth*, **107**, ETG 6-1–-25.

Koehn D, Passchier CW (2000) Shear sense indicators in striped bedding-veins. *Journal of Structural Geology*, **22**, 1141–51.

Lassey KR, Blattner P (1988) Kinetically controlled oxygen isotope exchange between fluid and rock in one-dimensional advective flow. *Geochimica et Cosmochimica Acta*, **52**, 2169–75.

Laubach SE, Ward ME (2006) Diagenesis in porosity evolution of opening-mode fractures, Middle Triassic to Lower Jurassic La Boca Formation, NE Mexico. *Tectonophysics*, **419**, 75–97.

Laubach SE, Lander RH, Bonnell LM, Olson JE, Reed RM (2004) Opening histories of fractures in sandstone. *Geological Society, London, Special Publications*, **231**, 1–9.

Lefticariu L, Perry EC, Fischer MP, Banner JL (2005) Evolution of fluid compartmentalization in a detachment fold complex. *Geology*, **33**, 69–72.

Leythaeuser D, Borromeo O, Mosca F, di Primio R, Radke M, Schaefer RG (1995) Pressure solution in carbonate source rocks and its control on petroleum generation and migration. *Marine and Petroleum Geology*, **12**, 717–33.

Lupa J, Flemings P, Tennant S (2002) Pressure and trap integrity in the deepwater Gulf of Mexico. *The Leading Edge*, **21**, 184–7.

Matter JM, Kelemen PB (2009) Permanent storage of carbon dioxide in geological reservoirs by mineral carbonation. *Nature Geoscience*, **2**, 837–41.

McCaig AM, Wayne DM, Marshall JD, Banks D, Henderson I (1995) Isotopic and fluid inclusion studies of fluid movement along the Gavarnie Thrust, central Pyrenees; reaction fronts in carbonate mylonites. *American Journal of Science*, **295**, 309–43.

Nollet S, Hilgers C, Urai J (2005) Sealing of fluid pathways in overpressure cells: a case study from the Buntsandstein in the Lower Saxony Basin (NW Germany). *International Journal of Earth Sciences*, **94**, 1039–55.

Odling NE, Gillespie P, Bourgine B, Castaing C, Chiles JP, Christensen NP, Fillion E, Genter A, Olsen C, Thrane L, Trice R, Aarseth E, Walsh JJ, Watterson J (1999) Variations in fracture system geometry and their implications for fluid flow in fractures hydrocarbon reservoirs. *Petroleum Geoscience*, **5**, 373–84.

Ohmoto H, Rye RO (1979) Isotopes of sulfur and carbon. In: *Geochemistry of Hydrothermal Ore Deposits* (ed. Barnes HL), pp. 509–67. John Wiley & Sons, New York.

Oliver J (1986) Fluids expelled tectonically from orogenic belts: their role in hydrocarbon migration and other geologic phenomena. *Geology*, **14**, 99–102.

Oliver NHS, Bons PD (2001) Mechanisms of fluid flow and fluid–rock interaction in fossil metamorphic hydrothermal systems inferred from vein–wallrock patterns, geometry and microstructure. *Geofluids*, **1**, 137–62.

Poupeau G, Saddiqi O, Michard A, Goffe B, Oberhansli R (1998) Late thermal evolution of the Oman Mountains subophiolitic windows: apatite fission-track thermochronology. *Geology*, **26**, 1139–42.

di Primio R, Leythaeuser D (1995) Quantification of the effect of carbonate redistribution by pressure solution in organic-rich carbonates. *Marine and Petroleum Geology*, **12**, 735–9.

Rabu D, Lemetour J, Bechennec F, Beurrier M, Villey M, Degrissac CB (1990) Sedimentary aspects of the Eo Alpine cycle on the northeast edge of the Arabian platform (Oman Mountains). In: *Geology and Tectonics of the Oman Region* (eds Robertson AHF, Searle MP, Ries AC), Geological Society, London, Special Publications, **49**, 49–68.

Ramsay JG (1980) The crack-seal mechanism of rock deformation. *Nature*, **284**, 135–9.

Renard F, Andréani M, Boullier A-M, Labaume P (2005) Crack-seal patterns: records of uncorrelated stress release variations in crustal rocks. *Geological Society, London, Special Publications*, **243**, 67–79.

Reuning L, Schoenherr J, Heimann A, Urai JL, Littke R, Kukla PA, Rawahi Z (2009) Constraints on the diagenesis, stratigraphy and internal dynamics of the surface-piercing salt domes in the Ghaba salt basin (Oman); a comparison to the Ara Group in the South Oman salt basin. *GeoArabia [Manama]*, **14**, 83–120.

Rickard MJ, Rixon LK (1983) Stress configurations in conjugate quartz-vein arrays. *Journal of Structural Geology*, **5**, 573–8.

Robertson A (1987) The transition from a passive margin to an Upper Cretaceous foreland basin related to ophiolite emplacement in the Oman Mountains. *Geological Society of America Bulletin*, **99**, 633–53.

Robertson AHF (1988) Late Cretaceous chemical sediments related to a carbonate platform-foreland basin transition in the Oman Mountains. *Sedimentary Geology*, **57**, 1–15.

Rye DM, Bradbury HJ (1988) Fluid flow in the crust; an example from a Pyrenean thrust ramp. *American Journal of Science*, **288**, 197–235.

Rygel AC, Anastasio DJ, Bebout GE (2006) Syntectonic infiltration by meteoric waters along the Sevier thrust front, southwest Montana. *Geofluids*, **6**, 288–301.

Scott RW (1990) Chronostratigraphy of the Cretaceous carbonate shelf, southeastern Arabia. *Geological Society, London, Special Publications*, **49**, 89–108.

Searle MP (2007) Structural geometry, style and timing of deformation in the Hawasina Window, Al Jebel al Akhdar and Saih Hatat culminations, Oman Mountains. *GeoArabia [Manama]*, **12**, 99–130.

Secor DT (1965) Role of fluid pressure in jointing. *American Journal of Science*, **263**, 633–46.

Sibson RH (1996) Structural permeability of fluid-driven fault-fracture meshes. *Journal of Structural Geology*, **18**, 1031–42.

Smith JW, Gould KW (1980) Isotopic study of the role of carbon dioxide in outbursts in coal mines. *Geochemical Journal*, **14**, 27–32.

Swarbrick RE, Osborne MJ, Yardley GS (2002) Comparison of overpressure magnitude resulting from the main generating mechanisms. In: *Pressure Regimes in Sedimentary Basins and their Prediction*, Vol. 76 (eds Huffman AR, Bowers GL), pp. 1–12. American Association of Petroleum Geologists Memoir, Tulsa, OK.

Terken JMJ (1999) The Natih petroleum system of North Oman. *GeoArabia [Manama]*, **4**, 157–80.

Terken JMJ, Frewin NL, Indrelid SL (2001) Petroleum systems of Oman: charge timing and risks. *AAPG Bulletin*, **85**, 1817–45.

Urai JL, Williams PF, van Roermund HLM (1991) Kinematics of crystal growth in syntectonic fibrous veins. *Journal of Structural Geology*, **13**, 823–36.

Urai JL, Spaeth G, van der Zee W, Hilgers C (2001) Evolution of mullion (formerly boudin) structures in the Variscan of the Ardennes and Eifel. *Journal of the Virtual Explorer*, **03**, paper 1, doi: 10.3809/jvirtex.2001.00027.

Valley JW, O'Neil JR (1981) 13C12C exchange between calcite and graphite: a possible thermometer in Grenville marbles. *Geochimica et Cosmochimica Acta*, **45**, 411–9.

Van Noten K, Hilgers C, Urai JL, Sintubin M (2008) Late burial to early tectonic quartz veins in the periphery of the high-Ardenne slate belt (Rursee, north Eifel, Germany). *Geologica Belgica*, **11**, 179–98.

Van Noten K, Van Baelen H, Sintubin M (2012) The complexity of 3D stress-state changes during compressional tectonic inversion at the onset of orogeny. *Geological Society, London, Special Publications*, **367**, 51–69.

Veizer J, Ala D, Azmy K, Bruckschen P, Buhl D, Bruhn F, Carden GAF, Diener A, Ebneth S, Godderis Y, Jasper T, Korte C, Pawellek F, Podlaha OG, Strauss H (1999) $^{87}Sr/^{86}Sr$, $\delta^{13}C$ and $\delta\ ^{18}O$ evolution of Phanerozoic seawater. *Chemical Geology*, **161**, 59–88.

Vermilye JM, Scholz CH (1995) Relation between vein length and aperture: J M. Vermilye & C. H. Scholz. *Journal of Structural Geology*, **17**, 423–34.

Virgo S, Arndt M (2010) Evolution of a crack-seal calcite vein network in limestone: a high resolution structural, microstructural and geochemical study from the Jebel Akhdar high pressure cell, Oman Mountains. Diplom Thesis. Lehr- und Forschungsgebiet Geologie - Endogene Dynamik. RWTH-Aachen University.

Virgo S, Abe S, Urai JL (2013a) Extension fracture propagation in rocks with veins: insight into the crack-seal process using discrete element method modeling. *Journal of Geophysical Research-Solid Earth*, **118**, 5236–51.

Virgo S, Arndt M, Sobisch Z, Urai JL (2013b) Development of fault and vein networks in a carbonate sequence near Hayl al-Shaz, Oman Mountains. *GeoArabia [Manama]*, **18**, 99–136.

Wagner PD (1990) Geochemical stratigraphy and porosity controls in Cretaceous carbonates near the Oman Mountains. *Geological Society, London, Special Publications*, **49**, 127–37.

Walsh JJ, Bailey WR, Childs C, Nicol A, Bonson CG (2003) Formation of segmented normal faults: a 3-D perspective. *Journal of Structural Geology*, **25**, 1251–62.

Wiltschko DV, Morse JW (2001) Crystallization pressure versus 'crack seal' as the mechanism for banded veins. *Geology*, **29**, 79–82.

Wiltschko DV, Lambert GR, Lamb W (2009) Conditions during syntectonic vein formation in the footwall of the Absaroka Thrust Fault, Idaho–Wyoming–Utah fold and thrust belt. *Journal of Structural Geology*, **31**, 1039–57.

Wohlwend S, Weissert H (2012) In search of mid-Cretaceous ocean anoxic events in Oman, an equatorial southern margin of the Tethys and the window into the Indo-Pacific. In: Geophysical Research Abstracts Vienna, EGU, 14, EGU2012-3144.